arXiv:hep-ex/0201003 v1 3 Jan 2002

DESY-01-222
January 3, 2002

Search for lepton-flavor violation in e^+p collisions at HERA

ZEUS Collaboration

Abstract

A search has been made for lepton-flavor-violating interactions of the type $e^+p \to \ell X$, where ℓ denotes a μ or τ with high transverse momentum, at a center-of-mass energy, $\sqrt{s}$, of 300 GeV with an integrated luminosity of $47.7\,\mathrm{pb}^{-1}$ using the ZEUS detector at HERA. No evidence was found for lepton-flavor violation and constraints were derived on leptoquarks (LQs) that could mediate such interactions. For LQ masses below $\sqrt{s}$, limits are set on $\lambda_{eq_1}\sqrt{\beta_{\ell q}}$, where λ_{eq_1} is the coupling of the LQ to an electron and a first-generation quark q_1 and $\beta_{\ell q}$ is the branching ratio of the LQ to ℓ and a quark. For LQ masses exceeding $\sqrt{s}$, limits are set on the four-fermion contact-interaction term $\lambda_{eq_\alpha}\lambda_{\ell q_\beta}/M^2_{\mathrm{LQ}}$ for leptoquarks that couple to an electron and a quark q_α and also to ℓ and a quark q_β. Some of the limits are also applicable to lepton-flavor-violating processes mediated by squarks in R-parity-violating supersymmetric models. In some cases involving heavy quarks and especially for $\ell = \tau$, the ZEUS limits are the most stringent published to date.

The ZEUS Collaboration

S. Chekanov, M. Derrick, D. Krakauer, S. Magill, B. Musgrave, A. Pellegrino, J. Repond, R. Yoshida
Argonne National Laboratory, Argonne, Illinois 60439-4815

M.C.K. Mattingly
Andrews University, Berrien Springs, Michigan 49104-0380

P. Antonioli, G. Bari, M. Basile, L. Bellagamba, D. Boscherini, A. Bruni, G. Bruni, G. Cara Romeo, L. Cifarelli, F. Cindolo, A. Contin, M. Corradi, S. De Pasquale, P. Giusti, G. Iacobucci, G. Levi, A. Margotti, T. Massam, R. Nania, F. Palmonari, A. Pesci, G. Sartorelli, A. Zichichi
University and INFN Bologna, Bologna, Italy

G. Aghuzumtsyan, D. Bartsch, I. Brock, J. Crittenden[1], S. Goers, H. Hartmann, E. Hilger, P. Irrgang, H.-P. Jakob, A. Kappes, U.F. Katz[2], R. Kerger, O. Kind, E. Paul, J. Rautenberg[3], R. Renner, H. Schnurbusch, A. Stifutkin, J. Tandler, K.C. Voss, A. Weber, H. Wessoleck
Physikalisches Institut der Universität Bonn, Bonn, Germany

D.S. Bailey[4], N.H. Brook[4], J.E. Cole, B. Foster, G.P. Heath, H.F. Heath, S. Robins, E. Rodrigues[5], J. Scott, R.J. Tapper, M. Wing
H.H. Wills Physics Laboratory, University of Bristol, Bristol, United Kingdom

M. Capua, A. Mastroberardino, M. Schioppa, G. Susinno
Calabria University, Physics Department and INFN, Cosenza, Italy

H.Y. Jeoung, J.Y. Kim, J.H. Lee, I.T. Lim, K.J. Ma, M.Y. Pac[6]
Chonnam National University, Kwangju, Korea

A. Caldwell, M. Helbich, X. Liu, B. Mellado, S. Paganis, W.B. Schmidke, F. Sciulli
Nevis Laboratories, Columbia University, Irvington on Hudson, New York 10027

J. Chwastowski, A. Eskreys, J. Figiel, K. Olkiewicz, M.B. Przybycień[7], P. Stopa, L. Zawiejski
Institute of Nuclear Physics, Cracow, Poland

B. Bednarek, I. Grabowska-Bold, K. Jeleń, D. Kisielewska, A.M. Kowal[8], M. Kowal, T. Kowalski, B. Mindur, M. Przybycień, E. Rulikowska-Zarębska, L. Suszycki, D. Szuba, J. Szuba[9]
Faculty of Physics and Nuclear Techniques, University of Mining and Metallurgy, Cracow, Poland

A. Kotański, W. Słomiński[10]
Department of Physics, Jagellonian University, Cracow, Poland

L.A.T. Bauerdick[11], U. Behrens, K. Borras, V. Chiochia, D. Dannheim, K. Desler[12], G. Drews, J. Fourletova, A. Fox-Murphy, U. Fricke, A. Geiser, F. Goebel, P. Göttlicher, R. Graciani, T. Haas, W. Hain, G.F. Hartner, S. Hillert, U. Kötz, H. Kowalski, H. Labes, D. Lelas, B. Löhr, R. Mankel, J. Martens[13], M. Martínez[11], M. Moritz, D. Notz, M.C. Petrucci, A. Polini, U. Schneekloth, F. Selonke, S. Stonjek, B. Surrow[14], J.J. Whitmore[15], R. Wichmann[16], G. Wolf, C. Youngman, W. Zeuner
Deutsches Elektronen-Synchrotron DESY, Hamburg, Germany

C. Coldewey[17], A. Lopez-Duran Viani, A. Meyer, S. Schlenstedt
DESY Zeuthen, Zeuthen, Germany

G. Barbagli, E. Gallo, C. Genta, P. G. Pelfer
University and INFN, Florence, Italy

A. Bamberger, A. Benen, N. Coppola, P. Markun, H. Raach, S. Wölfle
Fakultät für Physik der Universität Freiburg i.Br., Freiburg i.Br., Germany

M. Bell, P.J. Bussey, A.T. Doyle, C. Glasman, S. Hanlon, S.W. Lee, A. Lupi, G.J. McCance, D.H. Saxon, I.O. Skillicorn
Department of Physics and Astronomy, University of Glasgow, Glasgow, United Kingdom

B. Bodmann, U. Holm, H. Salehi, K. Wick, A. Ziegler, Ar. Ziegler
Hamburg University, I. Institute of Exp. Physics, Hamburg, Germany

T. Carli, I. Gialas[18], K. Klimek, E. Lohrmann, M. Milite
Hamburg University, II. Institute of Exp. Physics, Hamburg, Germany

C. Collins-Tooth, C. Foudas, R. Gonçalo[5], K.R. Long, F. Metlica, D.B. Miller, A.D. Tapper, R. Walker
Imperial College London, High Energy Nuclear Physics Group, London, United Kingdom

P. Cloth, D. Filges
Forschungszentrum Jülich, Institut für Kernphysik, Jülich, Germany

M. Kuze, K. Nagano, K. Tokushuku[19], S. Yamada, Y. Yamazaki
Institute of Particle and Nuclear Studies, KEK, Tsukuba, Japan

A.N. Barakbaev, E.G. Boos, N.S. Pokrovskiy, B.O. Zhautykov
Institute of Physics and Technology of Ministry of Education and Science of Kazakhstan, Almaty, Kazakhstan

S.H. Ahn, S.B. Lee, S.K. Park
Korea University, Seoul, Korea

H. Lim, D. Son
Kyungpook National University, Taegu, Korea

F. Barreiro, G. García, O. González, L. Labarga, J. del Peso, I. Redondo[20], J. Terrón, M. Vázquez
Departamento de Física Teórica, Universidad Autónoma Madrid, Madrid, Spain

M. Barbi, A. Bertolin, F. Corriveau, A. Ochs, S. Padhi, D.G. Stairs, M. St-Laurent
Department of Physics, McGill University, Montréal, Québec, Canada H3A 2T8

T. Tsurugai
Meiji Gakuin University, Faculty of General Education, Yokohama, Japan

A. Antonov, V. Bashkirov[21], P. Danilov, B.A. Dolgoshein, D. Gladkov, V. Sosnovtsev, S. Suchkov
Moscow Engineering Physics Institute, Moscow, Russia

R.K. Dementiev, P.F. Ermolov, Yu.A. Golubkov, I.I. Katkov, L.A. Khein, N.A. Korotkova, I.A. Korzhavina, V.A. Kuzmin, B.B. Levchenko, O.Yu. Lukina, A.S. Proskuryakov, L.M. Shcheglova, A.N. Solomin, N.N. Vlasov, S.A. Zotkin
Moscow State University, Institute of Nuclear Physics, Moscow, Russia

C. Bokel, J. Engelen, S. Grijpink, E. Koffeman, P. Kooijman, E. Maddox, S. Schagen, E. Tassi, H. Tiecke, N. Tuning, J.J. Velthuis, L. Wiggers, E. de Wolf
NIKHEF and University of Amsterdam, Amsterdam, Netherlands

N. Brümmer, B. Bylsma, L.S. Durkin, J. Gilmore, C.M. Ginsburg, C.L. Kim, T.Y. Ling
Physics Department, Ohio State University, Columbus, Ohio 43210

S. Boogert, A.M. Cooper-Sarkar, R.C.E. Devenish, J. Ferrando, T. Matsushita, M. Rigby, O. Ruske[22], M.R. Sutton, R. Walczak
Department of Physics, University of Oxford, Oxford United Kingdom

R. Brugnera, R. Carlin, F. Dal Corso, S. Dusini, A. Garfagnini, S. Limentani, A. Longhin, A. Parenti, M. Posocco, L. Stanco, M. Turcato
Dipartimento di Fisica dell' Università and INFN, Padova, Italy

L. Adamczyk[23], B.Y. Oh, P.R.B. Saull[23]
Department of Physics, Pennsylvania State University, University Park, Pennsylvania 16802

Y. Iga
Polytechnic University, Sagamihara, Japan

G. D'Agostini, G. Marini, A. Nigro
Dipartimento di Fisica, Università 'La Sapienza' and INFN, Rome, Italy

C. Cormack, J.C. Hart, N.A. McCubbin
Rutherford Appleton Laboratory, Chilton, Didcot, Oxon, United Kingdom

C. Heusch
University of California, Santa Cruz, California 95064

I.H. Park
Seoul National University, Seoul, Korea

N. Pavel
Fachbereich Physik der Universität-Gesamthochschule Siegen, Germany

H. Abramowicz, S. Dagan, A. Gabareen, S. Kananov, A. Kreisel, A. Levy
Raymond and Beverly Sackler Faculty of Exact Sciences, School of Physics, Tel-Aviv University, Tel-Aviv, Israel

T. Abe, T. Fusayasu, T. Kohno, K. Umemori, T. Yamashita
Department of Physics, University of Tokyo, Tokyo, Japan

R. Hamatsu, T. Hirose, M. Inuzuka, S. Kitamura[24], K. Matsuzawa, T. Nishimura
Tokyo Metropolitan University, Deptartment of Physics, Tokyo, Japan

M. Arneodo[25], N. Cartiglia, R. Cirio, M. Costa, M.I. Ferrero, S. Maselli, V. Monaco, C. Peroni, M. Ruspa, R. Sacchi, A. Solano, A. Staiano
Università di Torino, Dipartimento di Fisica Sperimentale and INFN, Torino, Italy

R. Galea, T. Koop, G.M. Levman, J.F. Martin, A. Mirea, A. Sabetfakhri
Department of Physics, University of Toronto, Toronto, Ontario, Canada M5S 1A7

J.M. Butterworth, C. Gwenlan, R. Hall-Wilton, M.E. Hayes[26], E.A. Heaphy, T.W. Jones, J.B. Lane, M.S. Lightwood, B.J. West
Physics and Astronomy Department, University College London, London, United Kingdom

J. Ciborowski[27], R. Ciesielski, G. Grzelak, R.J. Nowak, J.M. Pawlak, B. Smalska[28], J. Sztuk[29], T. Tymieniecka[30], A. Ukleja[30], J. Ukleja, J.A. Zakrzewski, A.F. Żarnecki
Warsaw University, Institute of Experimental Physics, Warsaw, Poland

M. Adamus, P. Plucinski
Institute for Nuclear Studies, Warsaw, Poland

Y. Eisenberg, L.K. Gladilin[31], D. Hochman, U. Karshon
Department of Particle Physics, Weizmann Institute, Rehovot, Israel

J. Breitweg[32], D. Chapin, R. Cross, D. Kçira, S. Lammers, D.D. Reeder, A.A. Savin, W.H. Smith
Department of Physics, University of Wisconsin, Madison, Wisconsin 53706

A. Deshpande, S. Dhawan, V.W. Hughes, P.B. Straub
Department of Physics, Yale University, New Haven, Connecticut 06520-8121

S. Bhadra, C.D. Catterall, S. Fourletov, S. Menary, M. Soares, J. Standage
Department of Physics, York University, Ontario, Canada M3J 1P3

[1] now at Cornell University, Ithaca/NY, USA
[2] on leave of absence at University of Erlangen-Nürnberg, Germany
[3] supported by the GIF, contract I-523-13.7/97
[4] PPARC Advanced fellow
[5] supported by the Portuguese Foundation for Science and Technology (FCT)
[6] now at Dongshin University, Naju, Korea
[7] now at Northwestern Univ., Evanston/IL, USA
[8] supported by the Polish State Committee for Scientific Research, grant no. 5 P-03B 13720
[9] partly supported by the Israel Science Foundation and the Israel Ministry of Science
[10] Department of Computer Science, Jagellonian University, Cracow
[11] now at Fermilab, Batavia/IL, USA
[12] now at DESY group MPY
[13] now at Philips Semiconductors Hamburg, Germany
[14] now at Brookhaven National Lab., Upton/NY, USA
[15] on leave from Penn State University, USA
[16] now at Mobilcom AG, Rendsburg-Büdelsdorf, Germany
[17] now at GFN Training GmbH, Hamburg
[18] Univ. of the Aegean, Greece
[19] also at University of Tokyo
[20] supported by the Comunidad Autonoma de Madrid
[21] now at Loma Linda University, Loma Linda, CA, USA
[22] now at IBM Global Services, Frankfurt/Main, Germany
[23] partly supported by Tel Aviv University
[24] present address: Tokyo Metropolitan University of Health Sciences, Tokyo 116-8551, Japan
[25] also at Università del Piemonte Orientale, Novara, Italy
[26] now at CERN, Geneva, Switzerland
[27] also at Łódź University, Poland
[28] supported by the Polish State Committee for Scientific Research, grant no. 2 P-03B 00219
[29] Łódź University, Poland
[30] sup. by Pol. State Com. for Scien. Res., 5 P-03B 09820 and by Germ. Fed. Min. for Edu. and Research (BMBF), POL 01/043
[31] on leave from MSU, partly supported by University of Wisconsin via the U.S.-Israel BSF
[32] now at EssNet Deutschland GmbH, Hamburg, Germany

1 Introduction

In the Standard Model (SM), lepton flavor is conserved. While the reported observation of neutrino oscillations [1, 2] implies that lepton-flavor violation (LFV) does occur, minimal extensions to the SM [3] that allow for finite neutrino masses and thereby account for neutrino oscillations do not predict detectable rates of LFV at current collider experiments. However, many extensions of the SM, such as grand unified theories [4], models based on supersymmetry [5], compositeness [6] or technicolor [7] involve LFV interactions at fundamental levels.

In high-energy positron–proton collisions at HERA, reactions of the type $eq_i \to \ell q_f$, where q_i and q_f denote initial- and final-state quarks and ℓ denotes a μ or a τ with high transverse momentum, can be detected with high efficiency and small background. Indirect searches for such reactions have yielded very strong constraints [8] for cases where q_i and q_f are light quarks. However, in some cases involving heavy quarks, especially when $\ell = \tau$, the sensitivity of HERA extends beyond existing low-energy limits.

This paper reports on a search for LFV processes in e^+p collisions using data collected by the ZEUS experiment from 1994 to 1997 with an integrated luminosity, $\mathcal{L}$, of $47.7\,\mathrm{pb}^{-1}$. Previous searches for LFV at HERA have been reported by ZEUS [9] ($\mathcal{L} \sim 4\,\mathrm{pb}^{-1}$) and H1 [10] ($\mathcal{L} \sim 37\,\mathrm{pb}^{-1}$).

2 Phenomenology

There are several mechanisms whereby lepton flavor can be violated in ep collisions. This paper considers two main possibilities: leptoquarks and R-parity-violating squarks.

2.1 Leptoquarks

Leptoquarks (LQs) are bosons that carry both lepton (L) and baryon (B) numbers and have lepton-quark Yukawa couplings. Such bosons arise naturally in unified theories that arrange quarks and leptons in common multiplets. A LQ that couples to leptons of two different generations would induce LFV. The Buchmüller-Rückl-Wyler (BRW) model [11], which assumes the most general Lagrangian with $\mathrm{SU(3)_C} \times \mathrm{SU(2)_L} \times \mathrm{U(1)_Y}$ invariant couplings of a LQ to a lepton and a quark, is used to classify LQ species and to calculate cross sections for LQ-mediated processes. The following additional assumptions were made to simplify the models under consideration:

1. one LQ species dominates the cross section of the process;

2. members of each SU(2) multiplet are degenerate in mass;

3. LQs couple to either left-handed or right-handed leptons, but not both.

There are 10 different LQ states in the BRW model, four of which can couple to both left- and right-handed leptons. Because of the third assumption above, models in which these states have left- or right-handed couplings will be treated separately in this analysis. Each state is characterized by spin $J = 0$ or 1, weak isospin $T = 0, 1/2$ or 1 and fermion number $F = 0$ or ± 2 (where $F = 3B + L$). Following the Aachen notation [12], scalar ($J = 0$) and vector ($J = 1$) LQs are denoted S_T^χ and V_T^χ, respectively, where $\chi = L, R$ denotes the chirality of the lepton that couples to the LQ. When two different hypercharge states are allowed, one is distinguished by a tilde. In this paper, LQs with couplings λ_{eq_α} to an electron and a quark q_α, and $\lambda_{\ell q_\beta}$ to a lepton ℓ (μ or τ) and a quark q_β, are considered[1]. The subscripts α and β label the quark generations. The LQ species determines whether q_α or q_β are up- or down-type quarks. In addition to mediating LFV interactions, such LQs would also mediate flavor-conserving interactions with an e or a ν_e in the final state. These final states were not searched for in this analysis, but they were taken into account in calculating branching ratios (the same is true for final states with ν_μ or ν_τ).

In ep collisions, if the LQ mass, $M_{\rm LQ}$, is below $\sqrt{s}$ (low-mass LQs), the LQ is predominantly produced as an s-channel resonance, as shown in Fig. 1(a). In this case, only incident u or d quarks, denoted q_1, which couple to the incident positron to produce $F = 0$ LQs, are considered. In the e^+p data analyzed here, the production cross section for $F = 0$ LQs is much larger than for $F = -2$ LQs, assuming that $M_{\rm LQ}$ is sufficiently large so that the production is valence-quark dominated, since $F = -2$ LQs would be produced via $e^+\bar{q}$ fusion.

For small values of the Yukawa coupling, λ_{eq_1}, the resonance width becomes negligible and the s-channel Breit-Wigner line shape can be approximated (neglecting radiative effects) by a δ-function at $M_{\rm LQ} = \sqrt{xs}$, where x is the Bjorken variable in deep inelastic scattering (DIS). This leads to the Narrow Width Approximation (NWA)

$$\sigma_{T_3}^{NWA}(s, M_{\rm LQ}) = (J+1)\,\frac{\pi\lambda_{eq_1}^2}{4s} C_{T_3}\, q_1\left(x = \frac{M_{\rm LQ}^2}{s}, Q_0^2\right), \qquad (1)$$

where T_3 is the third component of the weak isospin, C_{T_3} is the square of the relevant SU(2) Clebsch-Gordan coefficient, and $q_1(x, Q_0^2)$ is the valence-quark density in the proton evaluated at the scale $Q_0^2 = M_{\rm LQ}^2$. The total production cross section for a given LQ is given by the sum over all states of the SU(2) multiplet that couple to a positron and a quark. The NWA becomes inaccurate if $q_1(x, Q_0^2)$ varies significantly with x on a scale

[1] Note that in the BRW model, some $\chi = L$ LQs also have neutrino-quark couplings; these couplings are fixed by $\mathrm{SU(2)_L}$ invariance to be equal to the corresponding charged lepton-quark couplings.

corresponding to the LQ width, $\Gamma_{LQ} \propto \lambda^2 M_{\rm LQ}$. In the present analysis, this occurs only when $M_{\rm LQ}$ is close to $\sqrt{s}$ ($x \to 1$). In this region, q_1 falls steeply with x and the convolution of q_1 with the Breit-Wigner line shape results in contributions to the cross section from quarks with x below the resonant peak. These non-resonant contributions to the cross section are neglected in the NWA. For LQs that couple to u (d) quarks, with $M_{\rm LQ} = 270\,{\rm GeV}$ ($250\,{\rm GeV}$) and $\lambda_{eq_1} = 0.3$, σ^{NWA} underestimates the cross section by $\simeq 20\%$. The rate for LFV events is proportional to $\sigma\beta_{\ell q}$ where $\beta_{\ell q}$ is the branching ratio to the ℓq final state. In this paper, the NWA is used to calculate cross sections for $M_{\rm LQ} < \sqrt{s}$, so that limits on $\sigma\beta_{\ell q}$ can be simply converted to limits on $\lambda_{eq_1}\sqrt{\beta_{\ell q}}$. The NWA underestimates the cross section, leading to conservative limits.

If $M_{\rm LQ} > \sqrt{s}$ (high-mass LQs), both s- and u-channel diagrams contribute, see Fig. 1. If $M_{\rm LQ} \gg \sqrt{s}$, the LQ propagator contracts to a four–fermion contact interaction and the cross section is proportional to $[\lambda_{eq_\alpha}\lambda_{\ell q_\beta}/M^2_{\rm LQ}]^2$. In this high-mass approximation (HMA), the cross section for an $F = 0$ LQ, in e^+p collisions, can be written as

$$\sigma^{HMA}_{F=0} = \frac{s}{32\pi}\left[\frac{\lambda_{eq_\alpha}\lambda_{\ell q_\beta}}{M^2_{\rm LQ}}\right]^2 \left[\int dx\,dy\,x\,q_\alpha(x,\hat{s})\,f(y) + \int dx\,dy\,x\,\bar{q}_\beta(x,-\hat{u})\,g(y)\right], \qquad (2)$$

with

$$f(y) = \begin{cases} 1/2 & \text{scalar LQ} \\ 2(1-y)^2 & \text{vector LQ} \end{cases}; \qquad g(y) = \begin{cases} (1-y)^2/2 & \text{scalar LQ} \\ 2 & \text{vector LQ} \end{cases},$$

where y is the inelasticity, $\hat{s} = sx$ and $\hat{u} = sx(y-1)$ are the scales at which the quark densities q_α and $\bar{q}_\beta$ are evaluated. The first and second integrals in (2) are due to the $s-$ and $u-$channel contributions, respectively ($|F| = 2$ LQs couple a quark in the u-channel and an anti-quark in the $s-$channel). The accuracy of the HMA increases with increasing LQ mass. For $M_{\rm LQ} > 600\,{\rm GeV}$, the minimum mass considered for this high-mass analysis, the accuracy is better than 10%.

In the high-mass case, LQ scenarios are characterized by the 14 LQ species, the three generations of q_α and q_β, and the two possible final-state leptons, leading to a total of 252 different LQ scenarios.

NLO QCD corrections [13,14] were applied only to the NWA production cross section for scalar LQs, since no calculation is available for vector LQs or for high-mass scalar LQs. These corrections increase the production cross section by $\simeq 15\%$ at $M_{\rm LQ} = 150\,{\rm GeV}$, increasing to $\simeq 30\%$ at $M_{\rm LQ} = 250\,{\rm GeV}$.

Corrections for QED initial-state radiation (ISR), evaluated using the Weizsäcker-Williams approximation [15,16], were applied to both the low- and high-mass cases. The QED ISR correction reduces the NWA cross section by $\sim 3\%$ at $M_{\rm LQ} = 150\,{\rm GeV}$ and by $\sim 25\%$

when $M_{\rm LQ}$ approaches the kinematic limit. For high-mass LQs, QED ISR corrections, evaluated at $M_{\rm LQ} = 600\,\text{GeV}$, were applied. They lower the cross section by less than 5%; the corrections decrease at higher masses.

2.2 *R*-parity-violating squarks

Supersymmetry (SUSY), which links bosons and fermions, is a promising extension to the SM. It assumes a supersymmetric partner for each SM particle, a bosonic partner for a fermion and vice-versa. R-parity is a multiplicative quantum number defined as $R_p = (-1)^{3B+L+2J}$. For SM particles, $R_p = 1$; for SUSY particles (sparticles), $R_p = -1$. In R_p-conserving processes, sparticles are pair produced and the lightest supersymmetric particle (LSP) is stable. In models with R_p violation ($\not{R}_p$), single SUSY-particle production is possible and the LSP decays into SM particles. Of special interest for HERA are $\not{R}_p$ Yukawa couplings that couple a squark (SUSY partner of a quark) to a lepton and a quark, which are described in the superpotential by the term [17] $\lambda'_{ijk} L^i Q^j \overline{D}^k$, where i, j and k are generation indices, L and Q denote the left-handed lepton and quark-doublet superfields, respectively and $\overline{D}$ denotes the right-handed quark-singlet chiral superfield. Expansion of the superfields using four-component Dirac notation yields

$$\mathcal{L} = \lambda'_{ijk} \left[-\tilde{e}^i_L u^j_L \overline{d}^k_R - e^i_L \tilde{u}^j_L \overline{d}^k_R - (\overline{e}^i_L)^c u^j_L (\tilde{d}^k_R)^* + \tilde{\nu}^i_L d^j_L \overline{d}^k_R + \nu^i_L \tilde{d}^j_L \overline{d}^k_R + (\overline{\nu}^i_L)^c d^j_L (\tilde{d}^k_R)^* \right] + \text{h. c.} \tag{3}$$

The superscript c denotes charge conjugation and the asterisk denotes complex conjugation of scalar fields. For $i = 1$, the second and third terms will result in $\tilde{u}^j$ and $\tilde{d}^k$ production in ep collisions. Identical terms appear in the Lagrangians for the scalar leptoquarks $\tilde{S}^L_{1/2}$ and S^L_0 [18]. The coupling λ'_{1j1} gives rise to the reaction $e^+ d \to \tilde{u}^j_L$, while the coupling λ'_{11k} would cause the reaction $e^- u \to \tilde{d}^k_R$.

Lepton-flavor violation would occur in models with two non-zero Yukawa couplings involving different lepton generations. For example, non-zero values of λ'_{1j1} and λ'_{ijk} $(i = 2, 3)$ would yield the process $e^+ d \to \tilde{u}^j \to \ell^+ d^k$, where $i = 2, 3$ corresponds to $\ell = \mu, \tau$. Squarks also undergo R_p-conserving decays to a quark and a gaugino, which were not considered in this analysis. Low-mass coupling limits on $\tilde{S}^L_{1/2}$ LQs can be interpreted, using $\lambda_{eq_1}\sqrt{\beta_{\ell q}} = \lambda'_{1j1}\sqrt{\beta_{\tilde{u}^j \to \ell q}}$, as limits on $\tilde{u}^j$ squarks that couple to eq_1 and to ℓq. In the low-mass case, the limits apply for any final-state quark q (except top). High-mass LQ limits can also be applied to squarks as described in Section 9.3.

3 The ZEUS detector

A detailed description of the ZEUS detector can be found elsewhere [19]. A brief outline of the components which are most relevant for this analysis is given below. Charged particles are tracked in the central tracking detector (CTD) [20], which operates in a magnetic field of 1.43 T provided by a thin superconducting coil. The CTD consists of 72 cylindrical drift chamber layers, organized in 9 superlayers covering the polar angle[2] region $15° < \theta < 164°$. The transverse-momentum resolution for full-length tracks is $\sigma(p_T)/p_T = 0.0058 p_T \oplus 0.0065 \oplus 0.0014/p_T$, with p_T in GeV. The CTD was used to reconstruct tracks of isolated muons and charged τ-decay products. It was also used to determine the interaction vertex with a typical resolution of 4 mm (1 mm) along (transverse to) the beam direction.

The high-resolution uranium–scintillator calorimeter (CAL) [21] consists of three parts: the forward (FCAL), the barrel (BCAL) and the rear (RCAL) calorimeters. The calorimeters are subdivided into towers each of which subtends a solid angle from 0.006 to 0.04 steradians. Each tower is longitudinally segmented into an electromagnetic (EMC) section and two hadronic (HAC) sections (one in RCAL). Each HAC section consists of a single cell, while the EMC section of each tower is further subdivided transversely into four cells (two in RCAL). The CAL energy resolutions, as measured under test-beam conditions, are $\sigma(E)/E = 0.18/\sqrt{E}$ for electrons and $\sigma(E)/E = 0.35/\sqrt{E}$ for hadrons (E in GeV). The arrival time of CAL energy deposits is measured with sub-nanosecond resolution for energy deposits above 4.5 GeV, allowing the rejection of non-ep background.

The FMUON detector [19] consists of layers of limited streamer tubes and drift-chamber planes located up to 10 m from the interaction point. The toroidal magnetic fields of the iron yoke (1.4 T) that surrounds the CAL and of two toroids (1.6 T) located about 9 m from the interaction point enable muon momentum measurements to be made. The FMUON tags high-momentum muons (muons with momenta below 5 GeV are unlikely to emerge from the FCAL) with polar angles in the range $8° < \theta < 20°$, extending well beyond the CTD acceptance.

The luminosity was measured by the luminosity detector (LUMI) from the rate of the Bethe-Heitler process $e^+p \to e^+\gamma p$ [22], where the photon is detected in a lead–scintillator calorimeter located at $Z = -107$ m in the HERA tunnel. The uncertainty on the luminosity measurement was 1.6%.

[2] The ZEUS coordinate system is a right-handed Cartesian system, with the Z axis pointing in the proton beam direction, referred to as the "forward direction", and the X axis pointing left towards the center of HERA. The coordinate origin is at the nominal interaction point. The pseudorapidity is defined as $\eta = -\ln\left(\tan\frac{\theta}{2}\right)$, where the polar angle, θ, is measured with respect to the proton beam direction.

4 Monte Carlo simulation

The simulation of the LQ signal, including both s- and u-channel processes, was performed using the generators LQMGEN 1.0 [23] (low-mass LQs) and LQGENEP 1.0 [24] (high-mass LQs) based on the BRW model [11]. Both generators are interfaced to JETSET 7.4 [25] to simulate hadronization and particle decays.

The following SM backgrounds were considered: charged current (CC) and neutral current (NC) deep inelastic scattering (DIS) were simulated using DJANGO6 2.4 [26], with the color–dipole model ARIADNE 4.08 [27] used to simulate the hadronic final state. Elastic and inelastic $\gamma\gamma \to \ell^+\ell^-$ reactions were simulated with LPAIR [28]. EPVEC 1.0 [29] was used to simulate W production. Photoproduction processes were simulated with HERWIG 5.8 [30]. The ZEUS detector and trigger were simulated with a program based on GEANT 3.13 [31]. The simulated events were processed by the same reconstruction programs as the data.

5 Kinematic quantities

Global calorimeter sums were calculated as follows: each calorimeter cell i with an energy deposit E_i above a threshold was assigned a four-momentum P^μ, defined as $P^\mu = (E_i, E_i \cos\phi_i \sin\theta_i, E_i \sin\phi_i \sin\theta_i, E_i \cos\theta_i)$, where ϕ_i and θ_i are the azimuthal and polar angles of the cell center relative to the event vertex. The total four-momentum deposited in the calorimeter (E, P_X, P_Y, P_Z) is given by the sum of the four-momenta for all cells. The transverse energy, E_t, is given by $\sum_i E_i \sin\theta_i$. The missing transverse momentum, $\not\!\!P_t$, is given by $\sqrt{P_X^2 + P_Y^2}$. The azimuth assigned to $\not\!\!P_t$, $\phi_{\rm miss}$, was defined by $\cos\phi_{\rm miss} = -P_X/\not\!\!P_t$ and $\sin\phi_{\rm miss} = -P_Y/\not\!\!P_t$. Jets used in identifying hadronic τ decays were reconstructed using an (η, ϕ) cone algorithm [32] with cone radius $R = 1$. The inputs to the jet algorithm were the four-momentum vectors of each calorimeter cell. The invariant mass of a jet, $M_{\rm jet}$, was calculated from the sum of all four-momentum vectors assigned to the jet. The transverse energy of a jet was denoted by $E_t^{\rm jet}$.

The $E - P_Z$ of the initial state is twice the positron beam energy, $2E_e = 55\,\text{GeV}$. For events that are fully contained in the calorimeter (ignoring particles escaping through the forward beam hole, which carry negligible $E - P_Z$), the measured $E - P_Z$ should be near $2E_e$. In photoproduction processes, where the final-state positron escapes through the rear beam hole, the $E - P_Z$ spectrum falls steeply, so that a cut on $E - P_Z$ is useful in reducing such backgrounds. Events with high-energy muons, which deposit only a small fraction of their energy in the calorimeter, will also have $E - P_Z$ substantially below $2E_e$. In the search for the $e \to \mu$ transition (see Sections 6.1 and 6.2), a cut was made on the

quantity $E - P_Z + \Delta_\mu$, where $\Delta_\mu = \not{P}_t(1 - \cos\theta_\mu)/\sin\theta_\mu$ is an estimate of the $E - P_Z$ carried by the muon, assuming that the transverse momentum of the muon is equal to $\not{P}_t$; θ_μ is the polar angle of the muon track.

6 Event selection for the $e \to \mu$ transition

Events from the reaction $ep \to \mu X$, mediated by a heavy LQ, would be characterized by a high-transverse-momentum (P_t) muon balanced by a jet. Since only a small fraction of the muon energy is deposited in the calorimeter, these events would have a large $\not{P}_t$. The offline event selection consisted of two steps: a pre-selection of events with $\not{P}_t$ and a final selection requiring an identified muon.

6.1 Pre-selection

The trigger, which is identical to that used in the CC DIS measurement described elsewhere [33], was based on a cut on $\not{P}_t$ with a considerably lower threshold than the selection cuts described below. After applying cuts to reject non-ep backgrounds (mainly cosmic rays and beam-gas interactions), the following pre-selection requirements were imposed:

- a reconstructed vertex with Z coordinate $|Z_{\rm VTX}| < 50\,{\rm cm}$;
- $\not{P}_t > 15\,{\rm GeV}$ and $\not{P}_t/\sqrt{E_t} > 2.5\sqrt{\rm GeV}$;
- $25\,{\rm GeV} < E - P_Z + \Delta_\mu < 100\,{\rm GeV}$;
- no electron with energy larger than 10 GeV.

The third cut discriminates against photoproduction events, while the fourth cut suppresses NC DIS. The electron finder [34] is based on a neural–network algorithm. After the pre–selection, 164 events remained, compared with 177.3 ± 3.8 events predicted by the SM simulation normalized to the integrated luminosity of the data. The error associated with the prediction arises from the generated MC statistics. The SM expectation is dominated by CC DIS, with small contributions from $ep \to e\mu^+\mu^- X$ and from W production. Simulated distributions of $E - P_Z + \Delta_\mu$, $\not{P}_t$, and $\not{P}_t/\sqrt{E_t}$ are compared with the data in Fig. 2. Good agreement is seen.

6.2 Muon identification

Two methods of muon identification were employed. The first, for very forward muons ($8^\circ < \theta_\mu < 20^\circ$), required a reconstructed track in the FMUON detector with azimuth

within 20° of $\phi_{\rm miss}$. In the second selection, for central muons ($15° < \theta_\mu < 164°$), the following CAL- and CTD-based requirements were imposed:

- a track that points to the vertex with transverse momentum ($P_t^{\rm trk}$) above 5 GeV and an azimuth that differs from $\phi_{\rm miss}$ by less than 20°;
- no additional tracks with azimuth within 50° of $\phi_{\rm miss}$ and $P_t^{\rm trk} > 1\,{\rm GeV}$;
- the calorimeter energy deposits are consistent with those expected from a minimum ionizing particle in an (η, ϕ) cone of radius $R = 0.3$, centered on the track;
- muons with $115° < \theta_\mu < 130°$ were excluded to eliminate the background from a very small fraction of electrons for which a large fraction of the energy was absorbed in the dead material between the BCAL and the RCAL.

After the muon identification, 2 events are left in the data, while the SM expectation is 1.43 ± 0.38, mainly from $ep \to e\mu^+\mu^- X$.

6.3 Final selection

The final selection was designed to reduce the SM background to a very low level. The following cuts were applied:

- $\not\!\!P_t > 20\,{\rm GeV}$;
- $\not\!\!P_t/\sqrt{E_t} > 4\sqrt{\rm GeV}$;
- $E - P_Z + \Delta_\mu > 30\,{\rm GeV}$.

No event survived these cuts, while 0.40 ± 0.18 events are predicted by SM processes, mostly from $ep \to e\mu^+\mu^- X$.

7 Event selection for the $e \to \tau$ transition

This channel is characterized by an isolated τ with high P_t balanced by a jet. Separate selections were made for hadronic τ decays (65%) and for the leptonic decays $\tau \to \ell\overline{\nu}_\ell\nu_\tau$ (35%). The same trigger as described in Section 6.1 was used. The offline event selection consisted of a pre-selection common to hadronic and leptonic τ decays and final selections specific to each decay mode of the τ. These mode-specific selections make use of the fact that one or more neutrinos are emitted in τ decay producing $\not\!\!P_t$ approximately aligned with the τ. To produce a reasonably large event sample to compare with SM predictions, the selections for each τ decay mode were done in two steps.

7.1 Pre-selection

In addition to cuts to reject non-ep background, the pre–selection requirements were:

- a reconstructed vertex with Z-coordinate $|Z_{\rm VTX}| < 50\,{\rm cm}$;
- $20\,{\rm GeV} < E - P_Z < 52\,{\rm GeV}$;
- energy in RCAL $< 7\,{\rm GeV}$.

The second cut reduces the photoproduction background. The third cut rejects NC DIS events where the positron was scattered into the RCAL.

7.2 Selection of hadronic τ decays

Events with a narrow 'pencil-like' jet consistent with hadronic τ decay were selected with the following requirements:

- the transverse energy of the jet associated with the τ should satisfy $E_t^{\tau-{\rm jet}} > 10\,{\rm GeV}$;
- $M_{\rm jet} < 7\,{\rm GeV}$;
- 1, 2 or 3 tracks associated with the jet;
- the number of calorimeter cells associated with the jet, $N_{\rm cells}$, is at least 10 (to suppress electrons) and at most 50 (to ensure that the jet is narrow);
- $R_{90\%} \leq 0.3$, where $R_{90\%}$ is the radius of the (η, ϕ)-cone centered on the jet axis that contains 90% of the jet energy;
- $f_{\rm EMC} < 0.95$, where $f_{\rm EMC}$ is the fraction of the jet energy deposited in the electromagnetic section of the calorimeter;
- $f_{\rm EMC} + f_{\rm LT} < 1.6$, where $f_{\rm LT}$ is the momentum of the most-energetic track in the jet divided by the jet energy (leading-track fraction).

The last two cuts reject electrons, for which $f_{\rm EMC} \sim 1$ and $f_{\rm LT} \sim 1$. After these cuts, 367 data events were selected in comparison to 377.7 ± 12.5 from the SM expectation (mainly from NC DIS, CC DIS and photoproduction). Figure 3 shows several distributions of characteristic variables of the τ candidates at this stage of the analysis. The SM simulation provides a reasonable description of the data.

The final stage of the hadronic τ-decay selection requires events consistent with a two-body τ+jet final state with an invariant mass above $\sim 100\,{\rm GeV}$:

- $E_t^{\tau-{\rm jet}} > 20\,{\rm GeV}$;
- the azimuthal angle of the τ candidate is within 20° of $\phi_{\rm miss}$;

- $\not\!\!P_t > 12\,\mathrm{GeV}$;
- at least one additional jet with $E_t^{\mathrm{jet}} > 25\,\mathrm{GeV}$.

No candidate satisfying these requirements was found, while 0.62 ± 0.18 events are expected from SM processes.

7.3 Selection of $\tau \to \mu\bar{\nu}_\mu\nu_\tau$ decays

After the pre-selection described in Section 7.1, events with an isolated high-P_t muon balanced by a jet were selected. Isolated muon candidates were identified using a neural-network algorithm that analyzed the pattern of longitudinal and transverse energy deposition in the calorimeter and matching track(s) in the CTD and/or the muon chambers. Since the energy deposited in the CAL by the muon is typically a small fraction of the energy of the τ, cuts on $\not\!\!P_t$ were applied. The initial requirements were:

- a muon with $P_t > 10\,\mathrm{GeV}$ and $8^\circ < \theta_\mu < 125^\circ$;
- $\not\!\!P_t > 15\,\mathrm{GeV}$;
- $\not\!\!P_t/\sqrt{E_t} > 4\sqrt{\mathrm{GeV}}$;
- a jet with $E_t^{\mathrm{jet}} > 25\,\mathrm{GeV}$;
- events with an identified electron [35] with energy greater than 10 GeV were vetoed.

The last cut reduces NC DIS background. Figures 4(a-b) show the distributions of $E - P_Z$ and $\not\!\!P_t$ for the $\tau \to \mu\bar{\nu}\nu$ candidates after these cuts, compared to the SM background. Good agreement is observed. After these cuts, 119 data events remained, compared to 107.2 ± 7.4 events from the SM expectation (mainly CC DIS and photoproduction).

The final selection consisted of two cuts:

- $\not\!\!P_t > 20\,\mathrm{GeV}$;
- the muon azimuth differs from ϕ_{miss} by less than 20°.

No event passed the final selection, while 0.23 ± 0.07 events were expected from SM processes.

7.4 Selection of $\tau \to e\bar{\nu}_e\nu_\tau$ decays

After the pre-selection described in Section 7.1, events with an isolated electron and a jet were selected by imposing the following requirements:

- an identified electron [35] with energy greater than 20 GeV and the polar angle θ_e satisfying $8^\circ < \theta_e < 125^\circ$;

- $\not\!\!P_t > 10\,\mathrm{GeV}$;
- $\not\!\!P_t/\sqrt{E_t} > 2\sqrt{\mathrm{GeV}}$;
- a jet with $E_t^{\mathrm{jet}} > 25\,\mathrm{GeV}$.

Figures 4(c-d) show the distributions of $E - P_Z$ and $\not\!\!P_t$ for the $\tau \to e\bar{\nu}\nu$ candidates that satisfied these requirements, where 116 data events were selected and 109.1 ± 5.4 events from SM backgrounds were expected (mainly NC DIS and photoproduction).

The final selection consisted of a higher $\not\!\!P_t$ cut and a requirement that the lepton and the jet be back-to-back:

- $\not\!\!P_t > 15\,\mathrm{GeV}$;
- the azimuth of the electron differs from ϕ_{miss} by less than 20°.

No event passed the final selection, while 0.32 ± 0.10 events were expected from SM processes.

8 Efficiencies

The selection efficiencies were evaluated using signal MC events (see Section 4). For resonant production of lepton-flavor-violating scalar LQs, the μ-channel selection efficiency falls from 60% to 52% as M_{LQ} increases from 140 GeV to 280 GeV, while the efficiency for vector LQs drops from 64% to 56%. For $M_{\mathrm{LQ}} > 240\,\mathrm{GeV}$, the FMUON-based muon selection increases the selection efficiency by about 20% compared to the CAL-CTD-based selection alone. Over the M_{LQ} interval from 140 GeV to 280 GeV, the selection efficiency for LQs that couple to τ increases from 24% to 31% for scalar LQs and from 21% to 33% for vector LQs.

For LQs with $M_{\mathrm{LQ}} \gg \sqrt{s}$, the efficiencies are almost independent of M_{LQ}, but depend strongly on the generation of the initial-state quark. For $e \to \mu$ transitions, the selection efficiency ranges from 15% to 45% for $F = 0$ LQs and from 15% to 35% for $|F| = 2$ LQs. For $e \to \tau$ transitions, the efficiencies are lower and range from 5% to 19% for $F = 0$ LQs and from 4% to 16% for $|F| = 2$ LQs. When the initial-state quark is a sea quark and especially for s, c, or b quarks, the efficiency is considerably lower than for valence quarks due to the softer x spectrum, which results in a lower transverse momentum for the final-state lepton.

9 Results

Since no candidate for LFV processes was found, limits were set on these processes. All limits were evaluated at 95% C.L. using a Bayesian approach, assuming a flat prior for the signal cross section. Systematic uncertainties in the detector simulation and in the integrated luminosity (see Section 9.1) were taken into account using a method described elsewhere [36]. For low-mass LQs with narrow width, the branching ratio, β, was regarded as a free parameter and limits were set on $\sigma\beta_{\ell q}$. These limits were converted to limits on $\lambda_{eq_1}\sqrt{\beta_{\ell q}}$ using (1) corrected for QED-ISR and NLO QCD (only for scalar LQs). For high-mass leptoquarks, the cross-section limit was converted to a limit on $\lambda_{eq_\alpha}\lambda_{\ell q_\beta}/M^2_{\rm LQ}$ using (2) with QED-ISR corrections. The CTEQ4 [37] parameterizations of parton densities were used to evaluate cross sections.

9.1 Systematic uncertainties

The uncertainty on the integrated luminosity is 1.6%. Systematic uncertainties of 3% on the CAL energy scale and 10% on the CAL response to muons were taken into account. The resulting variations on the efficiency for the muon (tau) channel were 3% (4%) for low-mass LQs and up to 15% (17%) for high-mass LQs that couple to b quarks in the initial state.

Systematic uncertainties in the cross-section evaluation, related to the choice of parton density function (PDF), were investigated using MRST [38] as an alternative choice to CTEQ4. The main differences were found for low-mass LQs with masses close to $\sqrt{s}$ when very high-x quarks are involved. In these cases, limits calculated using MRST were stricter than the CTEQ4-based limits presented here. Another possible source of uncertainties for vector and high-mass scalar LQs are the unknown NLO-QCD cross-section corrections (see Section 2.1).

9.2 Low-mass LQ and squark limits

Figure 5 shows upper limits on $\sigma\beta_{\mu q}$ and $\sigma\beta_{\tau q}$. For $e \to \mu$, the search is sensitive to processes with cross sections as low as 0.1 pb, while for $e \to \tau$, the sensitivity is $0.2-0.3$ pb. These limits apply generally to narrow resonances with LFV decay modes, for example, to the $\not{R}_p$ squarks described in Section 2.2.

Upper limits on $\lambda_{eq_1}\sqrt{\beta_{\ell q}}$ have been derived for F=0 LQs by assuming resonantly produced LQs described by the BRW model. These limits can be applied to processes involving any quark generations in the final state (excluding the $t-$quark). Figures 6(a-b)

show the upper limits on $\lambda_{eq_1}\sqrt{\beta_{\mu q}}$ for scalar and vector LQs, respectively. Under the assumption that $\lambda_{eq_1} = \lambda_{\mu q_\beta}$, limits on λ_{eq_1} can be derived. These are compared to limits from low-energy experiments in Figs. 6(c-d) for $\tilde{S}^L_{1/2}$ and V^R_0 LQs. These states do not couple to neutrinos and therefore $\beta_{\mu q} = 0.5$. For $M_{\rm LQ} < 250\,{\rm GeV}$, the ZEUS limits are stronger than the low-energy limits for LQs that couple to μ and b. Limits on $\lambda_{eq_1}\sqrt{\beta_{\tau q}}$ are shown in Figs. 7(a-b). Figures 7(c-d) show the corresponding limits on λ_{eq_1}, assuming $\lambda_{eq_1} = \lambda_{\tau q_\beta}$ (and therefore $\beta_{\tau q} = 0.5$). The ZEUS limits are more stringent than the limits from low-energy experiments over a wide mass range, with the exception of limits from $K^+ \to \pi^+\nu\bar{\nu}$ [39]. As described in Section 2.2, the limits on $\lambda_{eq_1}\sqrt{\beta_{\ell q}}$ for $\tilde{S}^L_{1/2}$ can be interpreted as limits on $\lambda'_{1j1}\sqrt{\beta_{\tilde{u}^j\to\ell q}}$ for $\tilde{u}^j$ squarks.

Another way to illustrate the sensitivity is to assume that the couplings have electromagnetic strength ($\lambda_{eq_1} = \lambda_{\ell q_\beta} = 0.3 \approx \sqrt{4\pi\alpha}$). In this case, LQs with masses up to 283 GeV are excluded, as shown in Table 1. Alternatively, as shown in Table 2, for a fixed $M_{\rm LQ}$ of 250 GeV, values of $\lambda_{eq_1}\sqrt{\beta_{\ell q}}$ down to 0.020 (0.027) for $LQ \to \mu q$ ($LQ \to \tau q$) are excluded.

The CDF [40] and DØ [41] collaborations exclude scalar LQs with $M_{\rm LQ} < 202\,{\rm GeV}$ and $M_{\rm LQ} < 200\,{\rm GeV}$, respectively, at 95% C.L. with $\beta_{\mu q} = 100\%$. CDF [42] excludes $M_{\rm LQ} < 99\,{\rm GeV}$ with $\beta_{\tau b} = 100\%$. The ZEUS limits are complementary to those of the Tevatron in the sense that the latter are independent of the Yukawa couplings and assume that LQs couple to a single lepton generation.

9.3 High-mass LQ and squark limits

For $M_{\rm LQ} \gg \sqrt{s}$, limits on $\lambda_{eq_\alpha}\lambda_{\ell q_\beta}/M^2_{\rm LQ}$ were evaluated for all combinations of quark generations (α, β). Tables 3 and 4 show these limits for $F = 0$ and $|F| = 2$ LQs, respectively, that couple to μq_β. Tables 5 and 6 show the corresponding limits for the LQs coupling to τq_β. In many cases involving c and b quarks, the ZEUS limits improve on the low-energy limits [8, 43, 44]. Limits obtained by H1 [10] are comparable to the ZEUS limits.

The limits on $\lambda_{eq_\alpha}\lambda_{\ell q_\beta}/M^2_{\rm LQ}$ for $\tilde{S}^L_{1/2}$ can be interpreted as limits on $\lambda'_{1j\alpha}\lambda'_{ij\beta}/M^2_{\tilde{u}}$ for a u-type squark of generation j, where $\ell = \mu$ or τ for $i = 2$ or 3, respectively. Similarly, the limits on S^L_0 LQs can be interpreted as limits on $\lambda'_{1\alpha k}\lambda'_{i\beta k}/M^2_{\tilde{d}}$ for a d-type squark of generation k.

10 Conclusions

A search for lepton-flavor violation has been performed with $47.7\,{\rm pb}^{-1}$ of e^+p data at $\sqrt{s} = 300\,{\rm GeV}$ collected with the ZEUS detector at HERA in 1994–1997. Both the μ and

τ channels have been analyzed. No evidence for LFV processes has been found.

Limits at 95% C.L. on cross sections, couplings and masses for F=0 LQs that mediate LFV processes have been set. Assuming the couplings $\lambda_{eq_1} = \lambda_{\ell q_\beta} = 0.3$, lower mass limits between 258 and 283 GeV have been derived for various LQs decaying to μq or τq. For $M_{\rm LQ} = 250\,{\rm GeV}$, upper limits for $\lambda_{eq_1}\sqrt{\beta_{\mu q}}$ in the range $(2.0-10)\cdot 10^{-2}$ and for $\lambda_{eq_1}\sqrt{\beta_{\tau q}}$ in the range $(2.7-15)\cdot 10^{-2}$ were obtained. Limits on $\tilde{S}^L_{1/2}$ also apply to up-type squarks that have R-parity-violating couplings to both a positron and either a μ or a τ.

For LQs with $M_{\rm LQ} \gg \sqrt{s}$, upper limits on $\lambda_{eq_\alpha}\lambda_{\ell q_\beta}/M^2_{\rm LQ}$ have been obtained and compared with bounds from low-energy experiments. Some of these limits also apply to high-mass R_p-violating squarks. A number of ZEUS limits are the most stringent published to date, especially for $e \to \tau$ transitions.

Acknowledgements

The strong support and encouragement of the DESY directorate have been invaluable. The experiment was made possible by the inventiveness and the diligent efforts of the HERA machine group. The design, construction and installation of the ZEUS detector have been made possible by the ingenuity and dedicated efforts of many people from inside DESY and from the home institutes who are not listed as authors. Their contributions are acknowledged with great appreciation. We acknowledge support by the following: the Natural Sciences and Engineering Research Council of Canada (NSERC); the German Federal Ministry for Education and Science, Research and Technology (BMBF), under contract numbers HZ1GUA 2, HZ1GUB 0, HZ1PDA 5, HZ1VFA 5; the MINERVA Gesellschaft für Forschung GmbH, the Israel Science Foundation, the U.S.-Israel Binational Science Foundation, the Israel Ministry of Science and the Benozyio Center for High Energy Physics; the German-Israeli Foundation, the Israel Science Foundation, and the Israel Ministry of Science; the Italian National Institute for Nuclear Physics (INFN); the Japanese Ministry of Education, Science and Culture (the Monbusho) and its grants for Scientific Research; the Korean Ministry of Education and Korea Science and Engineering Foundation; the Netherlands Foundation for Research on Matter (FOM); the Polish State Committee for Scientific Research, grant no. 115/E-343/SPUB-M/DESY/P-03/DZ 121/2001-2002 and by the German Federal Ministry for Education and Science, Research and Technology (BMBF); the Fund for Fundamental Research of Russian Ministry for Science and Education and by the German Federal Ministry for Education and Science, Research and Technology (BMBF); the Spanish Ministry of Education and Science through funds provided by CICYT; the Particle Physics and Astronomy Research Council, UK; the US Department of Energy; the US National Science Foundation.

References

[1] Super-Kamiokande Coll., Y. Fukuda et al., Phys. Rev. Lett. **81**, 1562 (1998).

[2] SNO Coll., Q.R. Ahmad et al., Phys. Rev. Lett. **87**, 071301 (2001).

[3] Z. Maki, M. Nakagawa and S. Sakata, Prog. Theor. Phys. **28**, 870 (1962);
P. Fisher, B. Kayser and K.S. McFarland, Ann. Rev. Nucl. Part. Sci. **49**, 481 (1999).

[4] J.C. Pati and A. Salam, Phys. Rev. **D 10**, 275 (1974);
H. Georgi and S.L. Glashow, Phys. Rev. Lett. **32**, 438 (1974);
P. Langacker, Phys. Rep. **72**, 185 (1981).

[5] H.P. Nilles, Phys. Rep. **110**, 1 (1984);
H.E. Haber and G.L. Kane, Phys. Rep. **117**, 75 (1985).

[6] B. Schrempp and F. Schrempp, Phys. Lett. **B 153**, 101 (1985);
J. Wudka, Phys. Lett. **B 167**, 337 (1986).

[7] S. Dimopoulos and L. Susskind, Nucl. Phys. **B 155**, 237 (1979);
S. Dimopoulos, Nucl. Phys. **B 168**, 69 (1980);
E. Farhi and L. Susskind, Phys. Rev. **D 20**, 3404 (1979);
E. Farhi and L. Susskind, Phys. Rep. **74**, 277 (1981).

[8] S. Davidson, D. Bailey and B.A. Campbell, Z. Phys. **C 61**, 613 (1994).

[9] ZEUS Coll., M. Derrick et al., Z. Phys. **C 73**, 613 (1997).

[10] H1 Coll., C. Adloff et al., Eur. Phys. J. **C 11**, 447 (1999). Erratum in Eur. Phys. J. C14, 553 (2000).

[11] W. Buchmüller, R. Rückl and D. Wyler, Phys. Lett. **B 191**, 442 (1987). Erratum in Phys. Lett. **B 448**, 320 (1999).

[12] A. Djouadi et al., Z. Phys. **C 46**, 679 (1990).

[13] T. Plehn et al., Z. Phys. **C 74**, 611 (1997).

[14] Z. Kunszt and W.J. Stirling, Z. Phys. **C 75**, 453 (1997).

[15] C. F. von Weizsäcker, Z. Phys. **88**, 612 (1934).

[16] E.J. Williams, Phys. Rev. **45**, 729 (1934).

[17] V. Barger, G.F. Giudice and T. Han, Phys. Rev. **D 40**, 2987 (1989).

[18] J. Butterworth and H. Dreiner, Nucl. Phys. **B 397**, 3 (1993).

[19] ZEUS Coll., U. Holm (ed.), *The ZEUS Detector*. Status Report (unpublished), DESY (1993), available on `http://www-zeus.desy.de/bluebook/bluebook.html`.

[20] N. Harnew et al., Nucl. Inst. Meth. **A 279**, 290 (1989);
B. Foster et al., Nucl. Phys. Proc. Suppl. **B 32**, 181 (1993);
B. Foster et al., Nucl. Inst. Meth. **A 338**, 254 (1994).

[21] M. Derrick et al., Nucl. Inst. Meth. **A 309**, 77 (1991);
A. Andresen et al., Nucl. Inst. Meth. **A 309**, 101 (1991);
A. Caldwell et al., Nucl. Inst. Meth. **A 321**, 356 (1992);
A. Bernstein et al., Nucl. Inst. Meth. **A 336**, 23 (1993).

[22] J. Andruszków et al., Report DESY-92-066, DESY, 1992;
ZEUS Coll., M. Derrick et al., Z. Phys. **C 63**, 391 (1994);
ZEUS Luminosity Group, J. Andruszków et al., Preprint DESY-01-041, 2001.

[23] S.B. Silverstein, *A Search for Nonresonant Effects of Leptoquarks in Electron-Proton Collisions*. Ph.D. Thesis, Wisconsin University, Madison, 1996. Unpublished.

[24] L. Bellagamba, Comp. Phys. Comm. **141**, 83 (2001).

[25] T. Sjöstrand, Comp. Phys. Comm. **82**, 74 (1994).

[26] K. Charchula, G.A. Schuler and H. Spiesberger, Comp. Phys. Comm. **81**, 381 (1994).

[27] L. Lönnblad, Comp. Phys. Comm. **71**, 15 (1992).

[28] J.A.M. Vermaseren, Nucl. Phys. **B 229**, 347 (1983).

[29] U. Baur, J.A.M. Vermaseren and D. Zeppenfeld, Nucl. Phys. **B 375**, 3 (1992).

[30] G. Marchesini et al., Comp. Phys. Comm. **67**, 465 (1992).

[31] R. Brun et al., GEANT3, Technical Report CERN-DD/EE/84-1, CERN, 1987.

[32] ZEUS Coll., J. Breitweg et al., Eur. Phys. J. **C 2**, 61 (1998).

[33] ZEUS Coll., J. Breitweg et al., Eur. Phys. J. **C 12**, 411 (2000).

[34] H. Abramowicz, A. Caldwell and R. Sinkus, Nucl. Inst. Meth. **A 365**, 508 (1995).

[35] ZEUS Coll., J. Breitweg et al., Eur. Phys. J. **C 11**, 427 (1999).

[36] M. Corradi, *Proceedings of the Workshop on Confidence Limits*, p. 237. Geneva, Switzerland, CERN (2000). Also in preprint CERN 2000-005, available on `http://cern.web.cern.ch/CERN/Divisions/EP/Events/CLW/PAPERS/PS/corradi.ps`.

[37] H.L. Lai et al., Phys. Rev. **D 55**, 1280 (1997).

[38] A.D. Martin et al., Eur. Phys. J. **C 4**, 463 (1998).

[39] E787 Coll., S. Adler et al., Phys. Rev. Lett. **84**, 3768 (2000).

[40] CDF Coll., F. Abe et al., Phys. Rev. Lett. **81**, 4806 (1998).

[41] DØ Coll., B. Abbott et al., Phys. Rev. Lett. **84**, 2088 (2000).

[42] CDF Coll., F. Abe et al., Phys. Rev. Lett. **78**, 2906 (1997).

[43] E. Gabrielli, Phys. Rev. **D 62**, 055009 (2000).

[44] Particle Data Group, D.E. Groom et al., Eur. Phys. J. **C 15**, 1 (2000).

LQ type	$\tilde{S}^L_{1/2}$	$S^L_{1/2}$	$S^R_{1/2}$	V^L_0	V^R_0	$\tilde{V}^R_0$	V^L_1
μ-channel limit on $M_{\rm LQ}$[GeV]	263	278	278	261	266	280	283
τ-channel limit on $M_{\rm LQ}$[GeV]	258	275	276	259	263	277	282

Table 1: *The 95% C.L. lower limits on $M_{\rm LQ}$ for the μ- and the τ-channels assuming $\lambda_{eq_1} = \lambda_{\ell q} = 0.3$.*

LQ type	$\tilde{S}^L_{1/2}$	$S^L_{1/2}$	$S^R_{1/2}$	V^L_0/V^R_0	$\tilde{V}^R_0$	V^L_1
μ-channel limit on $\lambda_{eq_1}\sqrt{\beta_{\mu q}}$	0.10	0.038	0.036	0.081	0.029	0.020
τ-channel limit on $\lambda_{eq_1}\sqrt{\beta_{\tau q}}$	0.15	0.054	0.051	0.10	0.038	0.027

Table 2: *The 95% C.L. upper limits on $\lambda_{eq_1}\sqrt{\beta_{\ell q}}$ for a leptoquark with mass $M_{\rm LQ} = 250\ GeV$.*

$e \to \mu$	ZEUS			$F = 0$			
$\alpha\beta$	$S^L_{1/2}$ e^+u_α	$S^R_{1/2}$ $e^+(u+d)_\alpha$	$\tilde{S}^L_{1/2}$ e^+d_α	V^L_0 e^+d_α	V^R_0 e^+d_α	$\tilde{V}^R_0$ e^+u_α	V^L_1 $e^+(\sqrt{2}u+d)_\alpha$
1 1	$\mu N \to eN$ 7.6×10^{-5} **1.9**	$\mu N \to eN$ 2.6×10^{-5} **1.6**	$\mu N \to eN$ 7.6×10^{-5} **2.9**	$\mu N \to eN$ 2.6×10^{-5} **1.9**	$\mu N \to eN$ 2.6×10^{-5} **1.9**	$\mu N \to eN$ 2.6×10^{-5} **1.5**	$\mu N \to eN$ 1.1×10^{-5} **0.7**
1 2	$D \to \mu\bar{e}$ 4 **1.9**	$K \to \mu\bar{e}$ 2.7×10^{-5} **1.6**	$K \to \mu\bar{e}$ 2.7×10^{-5} **3.0**	$K \to \mu\bar{e}$ 1.3×10^{-5} **2.3**	$K \to \mu\bar{e}$ 1.3×10^{-5} **2.3**	$D \to \mu\bar{e}$ 2 **1.7**	$K \to \mu\bar{e}$ 1.3×10^{-5} **0.8**
1 3	*	$B \to \mu\bar{e}$ 0.8 **3.1**	$B \to \mu\bar{e}$ 0.8 **3.1**	V_{ub} 0.2 **2.7**	$B \to \mu\bar{e}$ 0.4 **2.7**	*	V_{ub} 0.2 **2.7**
2 1	$D \to \mu\bar{e}$ 4 **8.5**	$K \to \mu\bar{e}$ 2.7×10^{-5} **4.9**	$K \to \mu\bar{e}$ 2.7×10^{-5} **6.2**	$K \to \mu\bar{e}$ 1.3×10^{-5} **2.8**	$K \to \mu\bar{e}$ 1.3×10^{-5} **2.8**	$D \to \mu\bar{e}$ 2 **3.2**	$K \to \mu\bar{e}$ 1.3×10^{-5} **1.5**
2 2	$\mu \to ee\bar{e}$ 5×10^{-3} **11**	$\mu \to ee\bar{e}$ 7.3×10^{-3} **5.5**	$\mu \to ee\bar{e}$ 1.6×10^{-2} **6.9**	$\mu \to ee\bar{e}$ 8×10^{-3} **3.4**	$\mu \to ee\bar{e}$ 8×10^{-3} **3.4**	$\mu \to ee\bar{e}$ 2.5×10^{-3} **5.1**	$\mu \to ee\bar{e}$ 1.5×10^{-3} **2.2**
2 3	*	$B \to \bar{\mu}eK$ 0.6 **8.8**	$B \to \bar{\mu}eK$ 0.6 **8.8**	$B \to \bar{\mu}eK$ 0.3 **5.7**	$B \to \bar{\mu}eK$ 0.3 **5.7**	*	$B \to \bar{\mu}eK$ 0.3 **5.7**
3 1	*	$B \to \mu\bar{e}$ 0.8 **9.3**	$B \to \mu\bar{e}$ 0.8 **9.3**	V_{ub} 0.2 **3.2**	$B \to \mu\bar{e}$ 0.4 **3.2**	*	V_{ub} 0.2 **3.2**
3 2	*	$B \to \bar{\mu}eK$ 0.6 **11**	$B \to \bar{\mu}eK$ 0.6 **11**	$B \to \bar{\mu}eK$ 0.3 **3.9**	$B \to \bar{\mu}eK$ 0.3 **3.9**	*	$B \to \bar{\mu}eK$ 0.3 **3.9**
3 3	*	$\mu \to ee\bar{e}$ 7.3×10^{-3} **16**	$\mu \to ee\bar{e}$ 1.6×10^{-2} **16**	$\mu \to ee\bar{e}$ 8×10^{-3} **8.0**	$\mu \to ee\bar{e}$ 8×10^{-3} **8.0**	*	$\mu \to ee\bar{e}$ 1.5×10^{-3} **8.0**

Table 3: *Upper limits at 95% C.L. on $\lambda_{eq_\alpha}\lambda_{\mu q_\beta}/M^2_{LQ}$ in units of TeV^{-2}, for $F = 0$ LQs that couple to eq_α and to μq_β. The columns correspond to the $F = 0$ LQ species. The eq_α combination for the s-channel case is reported under the LQ type. Each row corresponds to a different combination of quark generations (α, β) which couple to the positron and the μ, respectively. Within each cell, the measurement which provides the most stringent low–energy constraint is shown on the first line and the corresponding limit [8,43,44] is given on the second line. The ZEUS limits are shown on the third line of each cell (enclosed in a box when stronger than the low–energy constraint). The * indicates cases where a top quark must be involved.*

$e \to \mu$	ZEUS			$\lvert F\rvert = 2$			
$\alpha\beta$	S_0^L $e^+\bar{u}_\alpha$	S_0^R $e^+\bar{u}_\alpha$	$\tilde{S}_0^R$ $e^+\bar{d}_\alpha$	S_1^L $e^+(\bar{u}+\sqrt{2}\bar{d})_\alpha$	$V_{1/2}^L$ $e^+\bar{d}_\alpha$	$V_{1/2}^R$ $e^+(\bar{u}+\bar{d})_\alpha$	$\tilde{V}_{1/2}^L$ $e^+\bar{u}_\alpha$
1 1	$\mu N \to eN$ 7.6×10^{-5} **3.4**	$\mu N \to eN$ 7.6×10^{-5} **3.4**	$\mu N \to eN$ 7.6×10^{-5} **4.2**	$\mu N \to eN$ 2.3×10^{-5} **1.8**	$\mu N \to eN$ 2.6×10^{-5} **1.5**	$\mu N \to eN$ 1.3×10^{-5} **0.8**	$\mu N \to eN$ 2.6×10^{-5} **1.0**
1 2	$K \to \pi\nu\bar{\nu}$ 10^{-3} **7.1**	$D \to \mu\bar{e}$ 4 **7.1**	$K \to \mu\bar{e}$ 2.7×10^{-5} **5.6**	$K \to \mu\bar{e}$ 1.3×10^{-5} **2.6**	$K \to \mu\bar{e}$ 1.3×10^{-5} **3.1**	$K \to \mu\bar{e}$ 1.3×10^{-5} **2.5**	$D \to \mu\bar{e}$ 2 **4.4**
1 3	V_{ub} 0.4 *	*	$B \to \mu\bar{e}$ 0.8 **6.6**	V_{ub} 0.4 **3.2**	$B \to \mu\bar{e}$ 0.4 **4.7**	$B \to \mu\bar{e}$ 0.4 **4.7**	*
2 1	$K \to \pi\nu\bar{\nu}$ 10^{-3} **3.7**	$D \to \mu\bar{e}$ 4 **3.7**	$K \to \mu\bar{e}$ 2.7×10^{-5} **4.7**	$K \to \mu\bar{e}$ 1.3×10^{-5} **2.0**	$K \to \mu\bar{e}$ 1.3×10^{-5} **1.6**	$K \to \mu\bar{e}$ 1.3×10^{-5} **0.9**	$D \to \mu\bar{e}$ 2 **1.0**
2 2	$\mu \to ee\bar{e}$ 5×10^{-3} **11**	$\mu \to ee\bar{e}$ 5×10^{-3} **11**	$\mu \to ee\bar{e}$ 1.6×10^{-2} **6.9**	$\mu \to ee\bar{e}$ 1.3×10^{-2} **3.4**	$\mu \to ee\bar{e}$ 8×10^{-3} **3.4**	$\mu \to ee\bar{e}$ 3.7×10^{-3} **2.8**	$\mu \to ee\bar{e}$ 2.5×10^{-3} **5.1**
2 3	$B \to l\nu X$ 4 *	*	$B \to \bar{\mu}eK$ 0.6 **8.8**	$B \to \bar{\mu}eK$ 0.3 **4.4**	$B \to \bar{\mu}eK$ 0.3 **5.7**	$B \to \bar{\mu}eK$ 0.3 **5.7**	*
3 1	V_{ub} 0.4 *	*	$B \to \mu\bar{e}$ 0.8 **5.6**	V_{ub} 0.4 **2.8**	$B \to \mu\bar{e}$ 0.4 **1.6**	$B \to \mu\bar{e}$ 0.4 **1.6**	*
3 2	$B \to l\nu X$ 4 *	*	$B \to \bar{\mu}eK$ 0.6 **11**	$B \to \bar{\mu}eK$ 0.3 **5.6**	$B \to \bar{\mu}eK$ 0.3 **3.9**	$B \to \bar{\mu}eK$ 0.3 **3.9**	*
3 3	*	*	$\mu \to ee\bar{e}$ 1.6×10^{-2} **16**	$\mu \to ee\bar{e}$ 1.3×10^{-2} **8.2**	$\mu \to ee\bar{e}$ 8×10^{-3} **8.0**	$\mu \to ee\bar{e}$ 3.7×10^{-3} **8.0**	*

Table 4: *Upper limits at 95% C.L. on $\lambda_{eq_\alpha}\lambda_{\mu q_\beta}/M_{LQ}^2$ in units of* TeV^{-2}*, for $|F| = 2$ LQs that couple to eq_α and to μq_β. The columns correspond to the $|F| = 2$ LQ species. The format of the table is described in the caption of Table 3.*

$e \to \tau$	ZEUS			$F = 0$			
$\alpha\beta$	$S^L_{1/2}$ e^+u_α	$S^R_{1/2}$ $e^+(u+d)_\alpha$	$\tilde{S}^L_{1/2}$ e^+d_α	V^L_0 e^+d_α	V^R_0 e^+d_α	$\tilde{V}^R_0$ e^+u_α	V^L_1 $e^+(\sqrt{2}u+d)_\alpha$
1 1	$\tau \to \pi e$ 0.4 **3.0**	$\tau \to \pi e$ 0.2 **2.5**	$\tau \to \pi e$ 0.4 **4.6**	G_F 0.2 **3.3**	$\tau \to \pi e$ 0.2 **3.3**	$\tau \to \pi e$ 0.2 **2.4**	G_F 0.2 **1.2**
1 2	 **3.1**	$\tau \to Ke$ 5 **2.5**	$K \to \pi\nu\bar{\nu}$ 10^{-3} **4.7**	$\tau \to Ke$ 3 **3.7**	$\tau \to Ke$ 3 **3.7**	 **2.7**	$K \to \pi\nu\bar{\nu}$ 2.5×10^{-4} **1.3**
1 3	* 	$B \to \tau\bar{e}X$ 8 **5.1**	$B \to \tau\bar{e}X$ 8 **5.1**	$B \to l\nu X$ 2 **4.6**	$B \to \tau\bar{e}X$ 4 **4.6**	* 	$B \to l\nu X$ 2 **4.6**
2 1	 **16**	$\tau \to Ke$ 5 **9.2**	$K \to \pi\nu\bar{\nu}$ 10^{-3} **12**	$\tau \to Ke$ 3 **4.9**	$\tau \to Ke$ 3 **4.9**	 **6.2**	$K \to \pi\nu\bar{\nu}$ 2.5×10^{-4} **2.6**
2 2	$\tau \to ee\bar{e}$ 20 **20**	$\tau \to ee\bar{e}$ 30 **11**	$\tau \to ee\bar{e}$ 66 **12**	$\tau \to ee\bar{e}$ 33 **6.2**	$\tau \to ee\bar{e}$ 33 **6.2**	$\tau \to ee\bar{e}$ 10 **11**	$\tau \to ee\bar{e}$ 6.1 **4.3**
2 3	* 	$B \to \tau\bar{e}X$ 8 **16**	$B \to \tau\bar{e}X$ 8 **16**	$B \to l\nu X$ 2 **12**	$B \to \tau\bar{e}X$ 4 **12**	* 	$B \to l\nu X$ 2 **12**
3 1	* 	$B \to \tau\bar{e}X$ 8 **17**	$B \to \tau\bar{e}X$ 8 **17**	V_{ub} 0.2 **5.4**	$B \to \tau\bar{e}X$ 4 **5.4**	* 	V_{ub} 0.2 **5.4**
3 2	* 	$B \to \tau\bar{e}X$ 8 **22**	$B \to \tau\bar{e}X$ 8 **22**	$B \to l\nu X$ 2 **7.6**	$B \to \tau\bar{e}X$ 4 **7.6**	* 	$B \to l\nu X$ 2 **7.6**
3 3	* 	$\tau \to ee\bar{e}$ 30 **30**	$\tau \to ee\bar{e}$ 66 **30**	$\tau \to ee\bar{e}$ 33 **15**	$\tau \to ee\bar{e}$ 33 **15**	* 	$\tau \to ee\bar{e}$ 6.1 **15**

Table 5: *Upper limits at 95% C.L. on $\lambda_{eq_\alpha}\lambda_{\tau q_\beta}/M^2_{LQ}$ in units of TeV^{-2}, for $F = 0$ LQs that couple to eq_α and to τq_β. The columns correspond to the $F = 0$ LQ species. The format of the table is described in the caption of Table 3.*

$e \to \tau$	ZEUS			$\lvert F\rvert = 2$		
$\alpha\beta$	S_0^L $e^+\bar{u}_\alpha$	S_0^R $e^+\bar{u}_\alpha$	$\tilde{S}_0^R$ $e^+\bar{d}_\alpha$	S_1^L $e^+(\bar{u}+\sqrt{2}\bar{d})_\alpha$	$V_{1/2}^L$ $e^+\bar{d}_\alpha$	$V_{1/2}^R$ $e^+(\bar{u}+\bar{d})_\alpha$	$\tilde{V}_{1/2}^L$ $e^+\bar{u}_\alpha$
1 1	G_F 0.3 **5.4**	$\tau \to \pi e$ 0.4 **5.4**	$\tau \to \pi e$ 0.4 **7.1**	G_F 0.3 **2.8**	$\tau \to \pi e$ 0.2 **2.6**	$\tau \to \pi e$ 0.1 **1.3**	$\tau \to \pi e$ 0.2 **1.7**
1 2	$K \to \pi\nu\bar{\nu}$ 10^{-3} **14**	 **14**	$\tau \to Ke$ 5 **9.3**	$K \to \pi\nu\bar{\nu}$ 10^{-3} **4.6**	$K \to \pi\nu\bar{\nu}$ 5×10^{-4} **5.5**	$\tau \to Ke$ 3 **4.5**	 **8.2**
1 3	V_{ub} 0.4 *	 *	$B \to \tau\bar{e}X$ 8 **12**	V_{ub} 0.4 **5.5**	$B \to \tau\bar{e}X$ 4 **8.4**	$B \to \tau\bar{e}X$ 4 **8.4**	 *
2 1	$K \to \pi\nu\bar{\nu}$ 10^{-3} **5.9**	 **5.9**	$\tau \to Ke$ 5 **7.8**	$K \to \pi\nu\bar{\nu}$ 10^{-3} **3.2**	$K \to \pi\nu\bar{\nu}$ 5×10^{-4} **2.5**	$\tau \to Ke$ 3 **1.3**	 **1.6**
2 2	$\tau \to ee\bar{e}$ 20 **19**	$\tau \to ee\bar{e}$ 20 **19**	$\tau \to ee\bar{e}$ 66 **13**	$\tau \to ee\bar{e}$ 55 **6.2**	$\tau \to ee\bar{e}$ 33 **6.5**	$\tau \to ee\bar{e}$ 15 **5.2**	$\tau \to ee\bar{e}$ 10 **9.7**
2 3	$B \to l\nu X$ 4 *	 *	$B \to \tau\bar{e}X$ 8 **17**	$B \to l\nu X$ 4 **8.1**	$B \to \tau\bar{e}X$ 4 **11**	$B \to \tau\bar{e}X$ 4 **11**	 *
3 1	$B \to l\nu X$ 4 *	 *	$B \to \tau\bar{e}X$ 8 **9.3**	$B \to l\nu X$ 4 **4.7**	$B \to \tau\bar{e}X$ 4 **2.6**	$B \to \tau\bar{e}X$ 4 **2.6**	 *
3 2	$B \to l\nu X$ 4 *	 *	$B \to \tau\bar{e}X$ 8 **21**	$B \to l\nu X$ 4 **10.2**	$B \to \tau\bar{e}X$ 4 **7.6**	$B \to \tau\bar{e}X$ 4 **7.6**	 *
3 3	*	*	$\tau \to ee\bar{e}$ 66 **30**	$\tau \to ee\bar{e}$ 55 **16**	$\tau \to ee\bar{e}$ 33 **15**	$\tau \to ee\bar{e}$ 15 **15**	*

Table 6: *Upper limits at 95% C.L. on $\lambda_{eq_\alpha}\lambda_{\tau q_\beta}/M_{LQ}^2$ in units of TeV^{-2}, for $|F| = 2$ LQs that couple to eq_α and to τq_β. The columns correspond to the $|F| = 2$ LQ species. The format of the table is described in the caption of Table 3.*

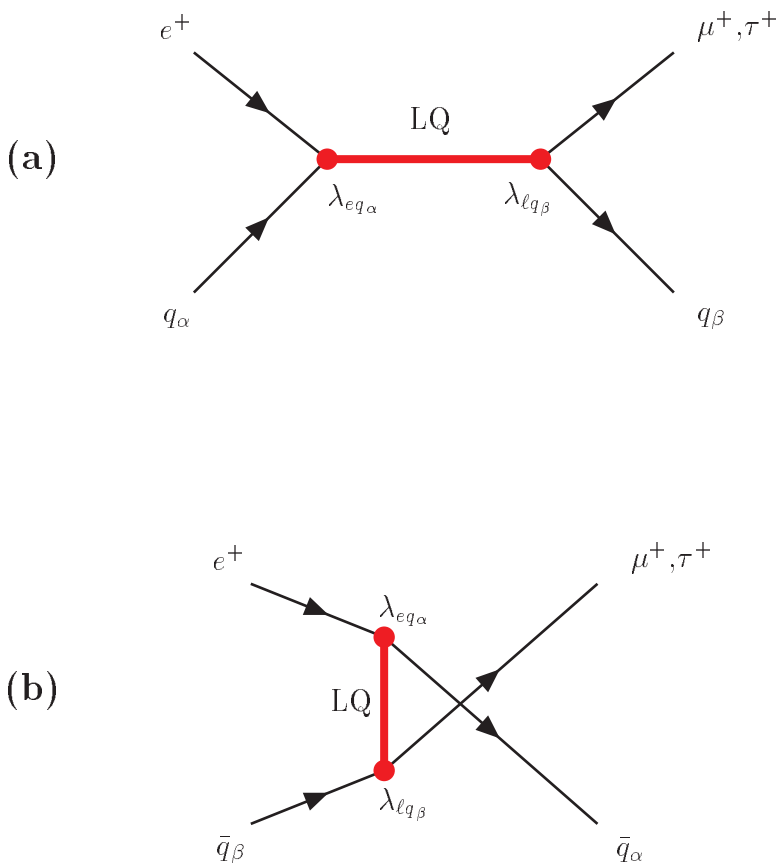

Figure 1: *(a) s-channel and (b) u-channel diagrams contributing to LFV processes induced by $F = 0$ LQs. In e^+p scattering, $|F| = 2$ LQs couple to antiquarks in the s-channel and to quarks in the u-channel.*

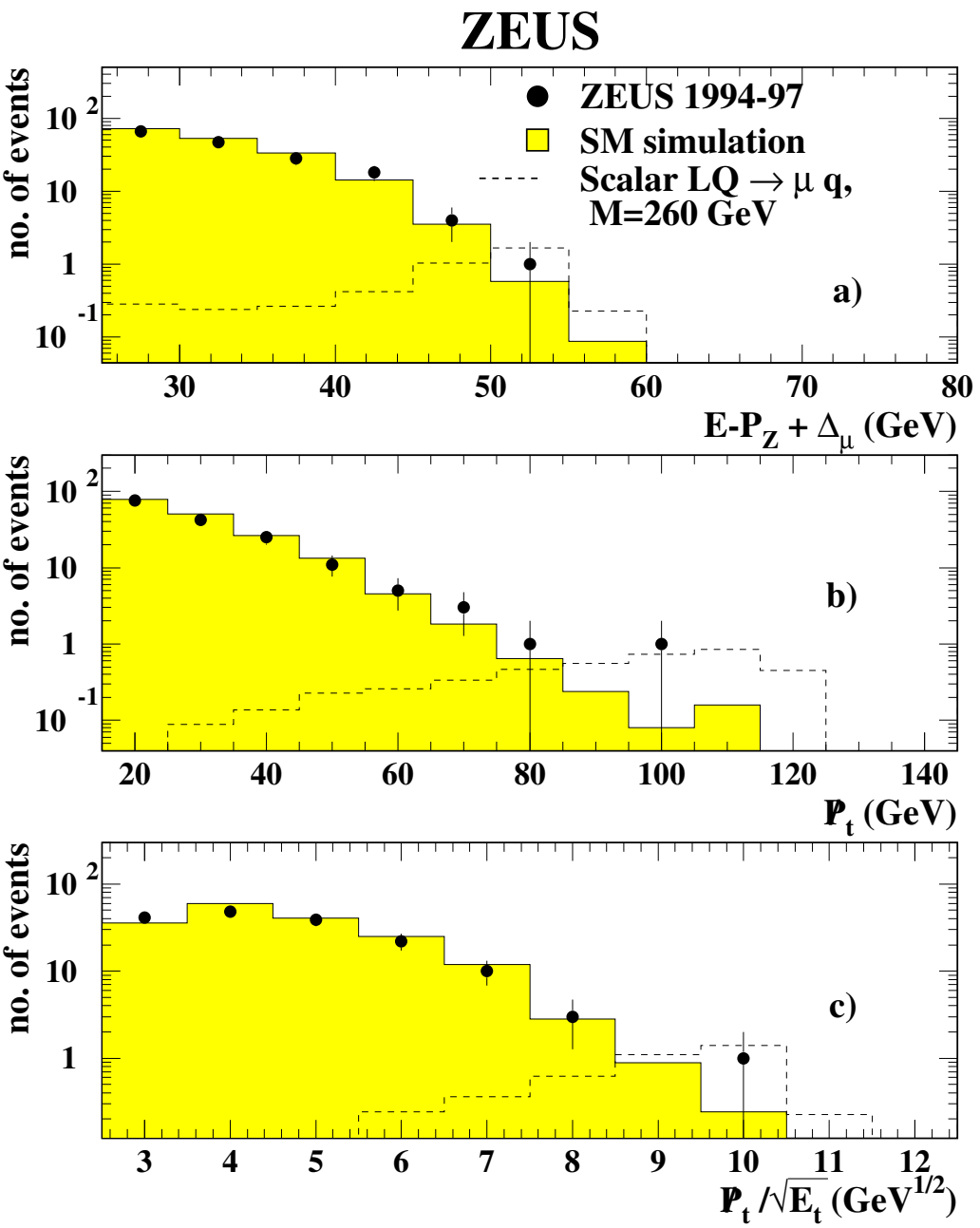

Figure 2: *Distributions of event variables after the μ-channel pre-selection for data (solid points) and SM simulation (shaded histograms) for a) $E - P_Z + \Delta_\mu$, b) $\not{P}_t$ and c) $\not{P}_t/\sqrt{E_t}$. The dashed histograms simulate the signal from a scalar LQ with $M_{\rm LQ} = 260\,GeV$ normalized to the 95% C.L. cross-section upper limit (see Section 9).*

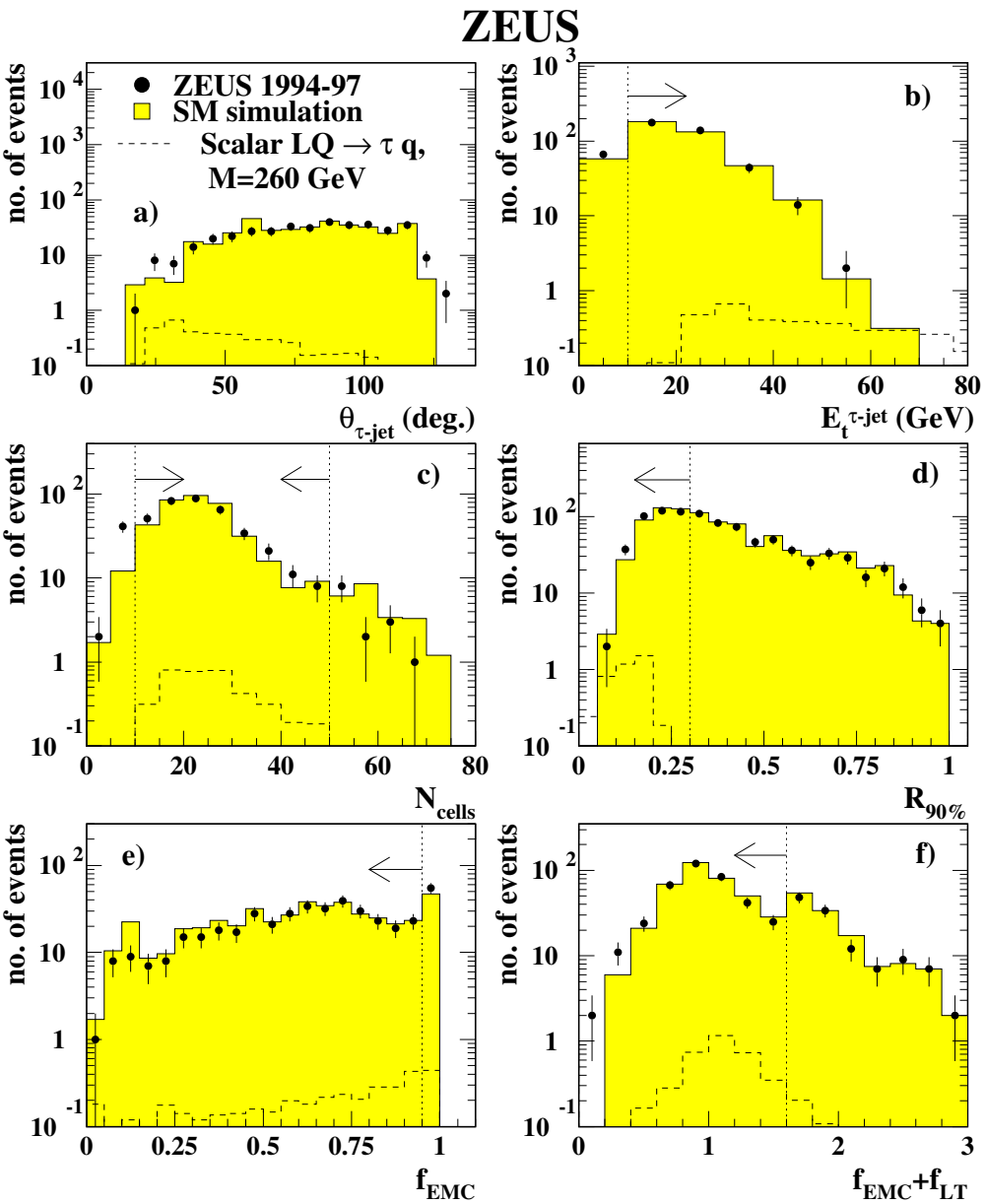

Figure 3: *Comparison of data (solid points) and simulated SM background (shaded histograms) for candidate jets from hadronic τ decays. The distributions are displayed for events that pass the selection cuts described in Section 7.2 except the ones imposed on the variable considered (indicated by the arrows). Shown are the distributions of: (a) $\theta_{\tau\text{-}jet}$, the polar angle of the τ candidate jet; (b) $E_t^{\tau\text{-}jet}$, the transverse energy; (c) $N_{\rm cells}$, the number of calorimeter cells belonging to the jet; (d) $R_{90\%}$, the (η,ϕ)-radius containing 90% of the jet energy; (e)$f_{\rm EMC}$, the fraction of the jet energy in the EMC section of the calorimeter; (f) $f_{\rm EMC}+f_{\rm LT}$ where $f_{\rm LT}$ is the momentum of the leading track divided by the jet energy. The SM backgrounds include NC and CC DIS, photoproduction, W production and $\gamma\gamma \to \tau^+\tau^-$. The dashed histograms simulate the signal from a scalar LQ with a mass of 260 GeV normalized to the 95% C.L. upper limit on the cross section (see Section 9).*

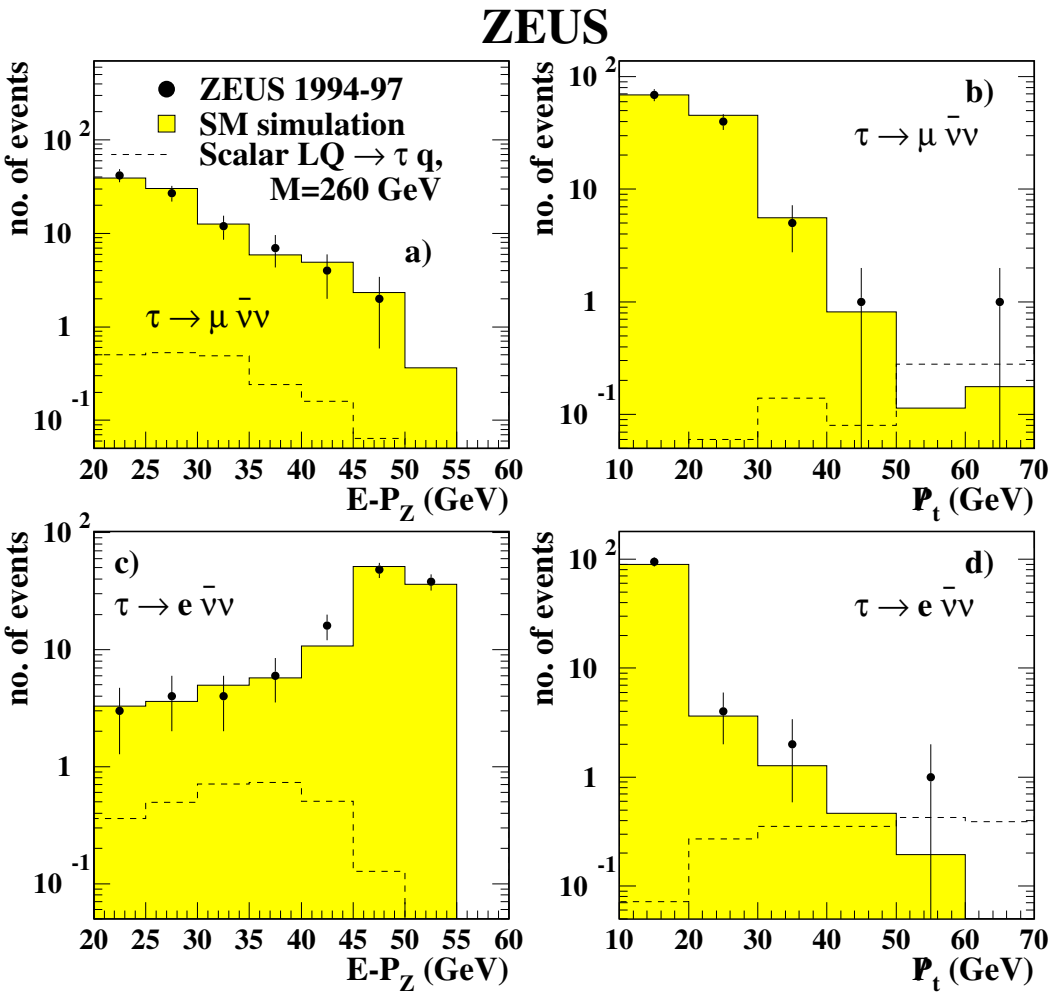

Figure 4: *Comparison of data (solid dots) with simulated SM background (shaded histogram) for the distributions of a) $E - P_Z$ and b) $\not{P}_t$ for the $\tau \to \mu\bar{\nu}\nu$ selection. The same distributions for the $\tau \to e\bar{\nu}\nu$ selection are shown in c) and d), respectively. The SM backgrounds include NC DIS, photoproduction, CC DIS, W production and $\gamma\gamma \to \tau^+\tau^-$. The dashed histograms simulate the signal from a scalar LQ with a mass of 260 GeV normalized to the 95% C.L. upper limit on the cross section (see Section 9).*

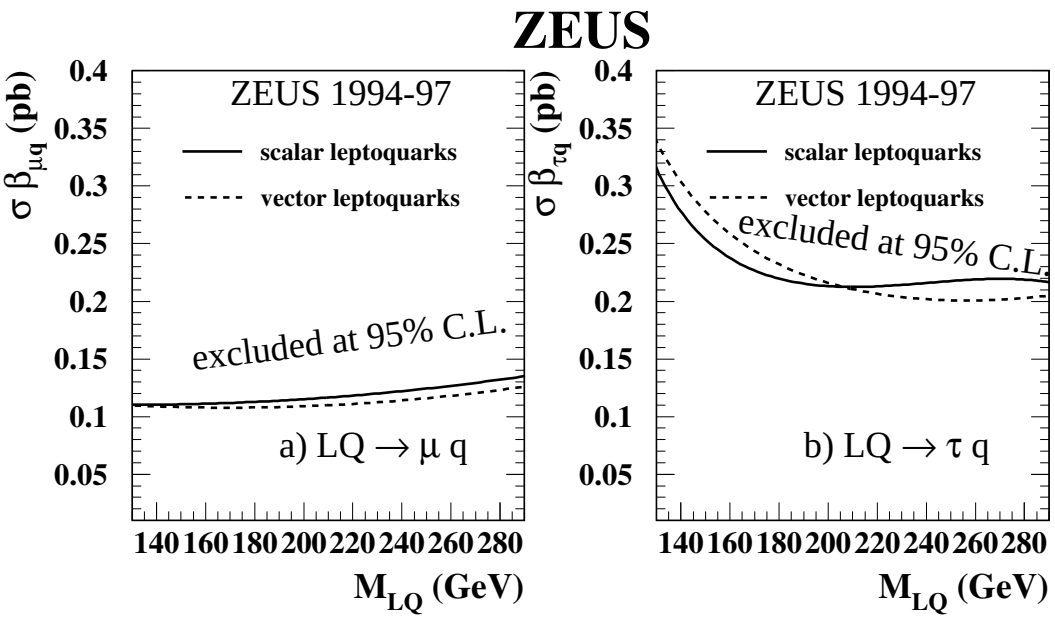

Figure 5: *The 95% C.L. upper limits on $\sigma\beta_{\ell q}$ as a function of $M_{\rm LQ}$ for scalar (full line) and vector (dashed line) LQs for a)* $\rm LQ \to \mu q$ *and b)* $\rm LQ \to \tau q$.

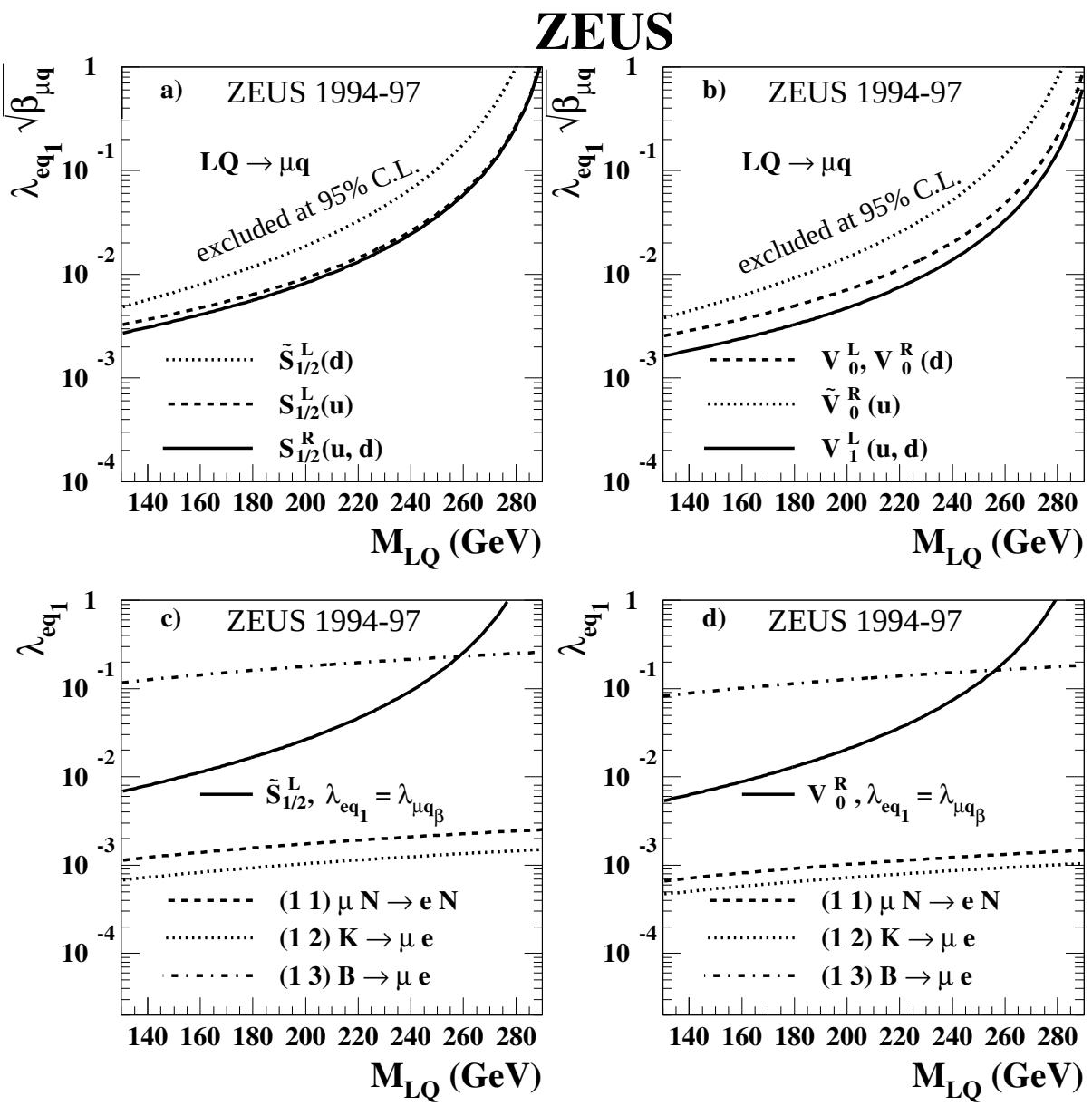

Figure 6: *Upper limits on $\lambda_{eq_1}\sqrt{\beta_{\mu q}}$ vs. $M_{\rm LQ}$ for a) scalar and b) vector LQs. The quark flavors that couple to the LQs in the initial state are shown in parentheses following the LQ species. Upper limits on λ_{eq_1} under the assumption $\beta_{\mu q} = 0.5$ are shown in c) for scalar LQs and d) for vector LQs that couple to d-type quarks. Also shown are existing limits [8,43,44] (dashed lines). The numbers in parentheses indicate the generations of the quarks that couple to the e and the μ, respectively. The regions above the curves are excluded at the 95% C.L.*

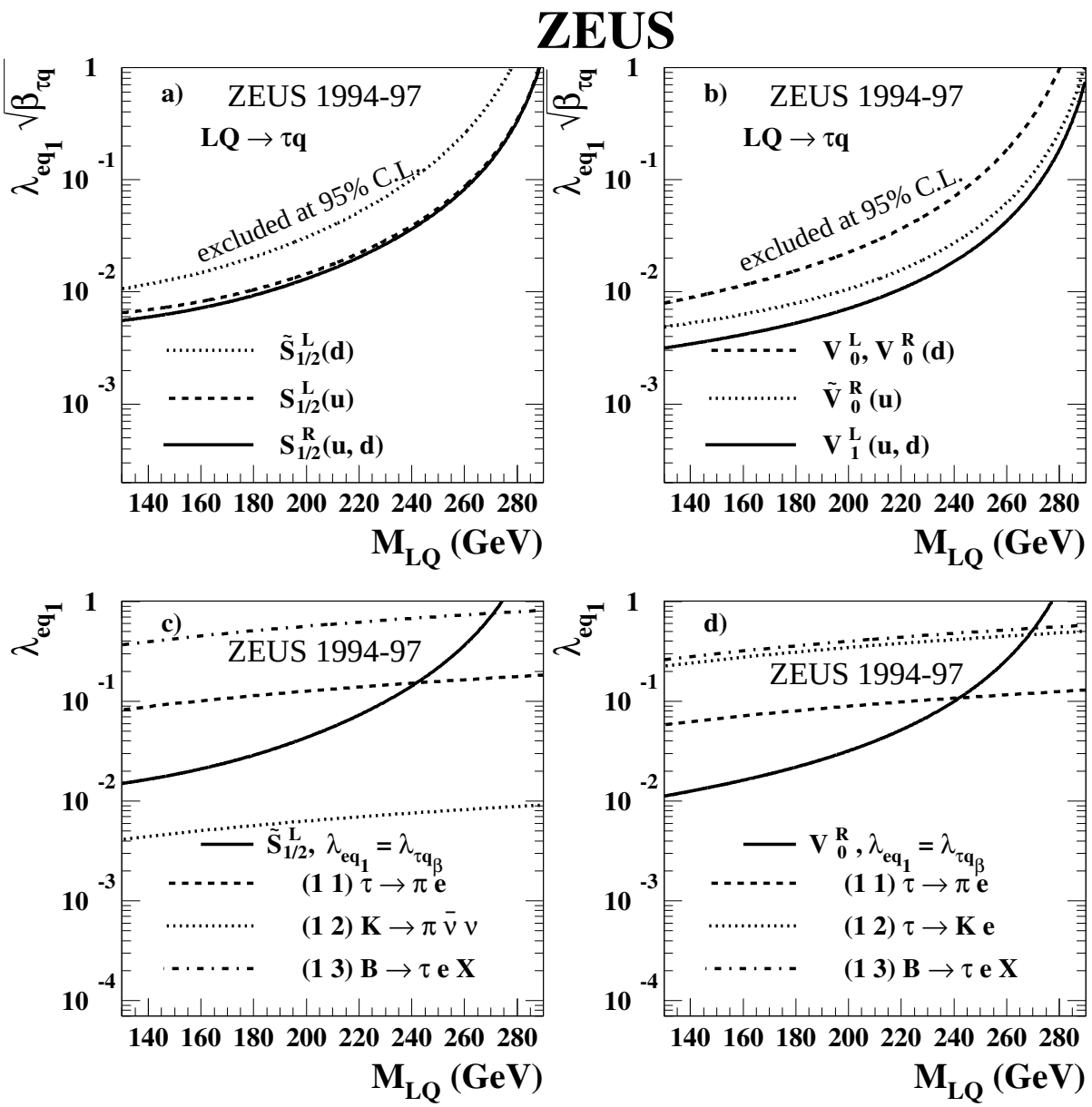

Figure 7: *Upper limits on $\lambda_{eq_1}\sqrt{\beta_{\tau q}}$ vs. $M_{\rm LQ}$ for a) scalar and b) vector LQs. The quark flavors that couple to the LQs in the initial state are shown in parentheses following the LQ species. Upper limits on λ_{eq_1} under the assumption $\beta_{\tau q} = 0.5$ are shown in c) for scalar LQs and d) for vector LQs that couple to d-type quarks. Also shown are existing limits [8,43,44] (dashed lines). The numbers in parentheses indicate the generations of the quarks that couple to the e and the τ, respectively. The regions above the curves are excluded at the 95% C.L.*